Exhumation of metamorphic core complexes through progressive doming and detachment faulting: insights from the Cretaceous Liaonan metamorphic core complex, eastern North China craton

Yuanyuan Zheng[1], Junlai Liu[1], Chunru Hou[1], Yanqi Sun[1], John P. Craddock[2]

[1]State Key Laboratory of Geological Processes and Mineral Resources, China University of Geosciences, Beijing 100083, China

[2]Geology Department, Macalester College, Saint Paul, Minnesota 55105, USA

Corresponding author: J. Liu (jliu@cugb.edu.cn)

Key Points:

- The characteristics and history of shearing are different between two branches of shear systems of the Liaonan metamorphic core complex.
- Subhorizontal shearing initiated at 138-134 Ma, followed by the detachment faulting from about 120 Ma along the master detachment fault.
- Progressive subhorizontal flow, doming and detachment faulting are possible mechanisms of exhumation of lower plate high grade rocks.

Abstract

To better understand the mechanisms of crustal exhumation related to tectonic extension, we report on the progressive doming and detachment faulting of the Cretaceous Liaonan metamorphic core complex (MCC). The detachment fault zone of Liaonan MCC is comprised of two branches, i.e., the Jinzhou detachment fault zone (JDFZ) and the poorly-researched Dongjiagou shear zone (DSZ). Thus, integrated structural, microstructural, quartz c-axis fabrics, and fluid inclusion analysis, and U-Pb on zircon dating were performed on mylonites along the DSZ. In contrast with the JDFZ that possesses characteristics of detachment fault zone, the DSZ encompasses Archean gneisses and Neoproterozoic meta-sedimentary rocks, between which exists an obvious metamorphic contrast forming a tectonic discontinuity contact (TDC). However, rocks from both sides of the TDC possess structures and fabrics for identical geometries and kinematics that are consistent with those along the JDFZ. Thermometric analysis of fluid inclusions from syn-tectonic quartz veins (630 °C, 470 °C, 350 °C) and quartz c-axis fabric from mylonites along the DSZ show that the shearing penetrates throughout the Archean to Neoproterozoic rocks. Dating of zircons from syn-kinematic granitic dikes from DSZ yields an age ca. 134 Ma, which is similar to the ages of early shearing along the JDFZ (ca. 133~134 Ma). The results imply that the shearing initiated in both JDFZ and DSZ at an early stage, then progressive shearing continued, and finally developed the detachment faulting along the JDFZ. Based on the timing and processes of the regional extension, a geodynamic model of MCC's is proposed.

1 Introduction

The concept of metamorphic core complex (MCC) was defined, from the study of Tertiary Cordilleran extensional tectonics, as a group of generally domal or archlike, isolated uplifts of anomalously deformed, metamorphic and plutonic rocks overlain by a tectonically detached and distended unmetamorphosed cover. (Davis & Coney, 1979; Coney, 1980). MCC's were identified subsequently in many Phanerozoic orogenic belts (e.g., Zheng et al., 1990; Vandenberg & Lister, 1996; Song, 1996; Darby et al., 2004; Liu et al., 2005; Cooper et al., 2010; Cao et al., 2013; Ni et al., 2013; Whitney et al., 2013), and early Precambrian terrains (e.g., Fu, 1992; Neumayr, 1998). It is generally accepted that a typical MCC contains three basic structural elements (Davis et al., 2002): (1) a master detachment fault zone with gentle dip and large displacement; (2) a lower plate of high grade gneisses intruded by syn-kinematic granitic plutons; and (3) faulted, but non-metamorphosed, supracrustal rocks and supradetachment basins in the upper plate. As the most prominent structural feature of MCC's, the detachment fault zone usually consists of a discontinuous brittle fault surface, underlain by a cataclasite zone, and mylonitic rocks. The latter are several hundred to several thousand meters thick and transit downward into the major metamorphic lower plate (Lister & Davis, 1989; Platt et al., 2014).

Although it is generally accepted that MCC's result from regional tectonic extension, the mechanisms of exhumation of the lower plates have been the focus of controversy over the last decades. A popularly cited model by Lister & Davis (1989)

consists of multi-generations of decollement. In their model, an initially sub-horizontal ductile shear zone at depth, decouples the middle to lower crust beneath a steeply-dipping array of normal faults in the upper plate. Low-angle normal faults are spawned from the zone, and the geometry of upper plate extension becomes increasingly complex. The lower plate bows upward with multiple detachment faults splaying from the developing domal culmination, as the result of unloading and isostatic effects of granite intrusion. The widely-accepted “rolling-hinge” model refers to the progressive flexural-isostatic shallowing of an initially steep fault during unloading of the footwall (e.g., Spencer, 1984; Buck, 1988; Wernicke & Axen, 1988). This model involves progressive back-tilting during exhumation of an originally moderate to steeply dipping fault that back-warps the footwall into an abandoned, domal structure while the fault remains active at depth (Mizera et al., 2019).

Exhumation of MCC’s may have close genetic relationships with regional doming in orogenic belt that sometimes MCC’s are considered as a type of dome structure. Even some typical gneiss domes were redefined as MCC’s (Platt et al., 2014). The distinction and relationship of MCC development and doming have therefore been topics of hot debates in recent years. Most of the cores in MCC’s are dome-shaped high-grade gneisses with migmatization. Some studies on MCC’s stressed the relationship of detachment faulting to the exhumation of lower plate rocks (Whitney et al., 2013). The Shuswap Complex in the hinterland of the Canadian Cordillera, for example, includes several domiform bodies cored by magmatic gneisses and granites, with foliations in the core gently dipping in association with normal faults. The normal faults showed features of detachment faults with estimated displacements greater than 30 km (Parrish et al., 1988). However, subsequent studies have shown that the temperatures of deformation of granitic gneisses and migmatites in the core reaches up to 750-800 °C (Norlander et al., 2002). The melts were shown to be the result of metamorphic origin due to isothermal decompression and partial melting (Norlander et al., 2002), crystallized at 50-60 Ma, and afterwards rapidly cooled at 56-48 Ma (Kruckenberg et al., 2008; Vanderhaeghe et al., 2003). It is suggested that during the isothermal decompression and crustal thinning, rapid delamination of crustal material resulted in a transition from gneiss dome formation to MCC exhumation (Teyssier & Whitney, 2002). It is therefore plausible that diapiric emplacement of hot lower crustal masses occurred in an early stage of exhumation.

Early Cretaceous extensional structures are widely distributed in the North China craton (NCC) and in eastern Asia (Figure 1a; Wang et al., 2011). The Liaonan MCC in the southern Liaodong peninsula was suggested to be a typical cordilleran type MCC that has a detachment fault zone of two branches (Figure 1b; Liu et al., 2005), i.e., the Jinzhou detachment fault zone (JDFZ) and Dongjiagou shear zone (DSZ). Previous studies confirmed that a thick sequence of fault rocks beneath the Jinzhou master detachment fault record progressive shearing along the JDFZ during exhumation of the lower plate. The DSZ, to the south of the lower plate, has been regarded as the eastward continuation of the JDFZ. Our observations reveal, however, that there are obvious contrasts in structural characteristics and deformation history between the JDFZ and the DSZ. In this study, structural, thermometric, fabric analysis and

geochronological dating of the poorly-studied DSZ help to elucidate the differences between the two, and thus evaluate their contribution to the exhumation of lower plate at the Liaonan MCC.

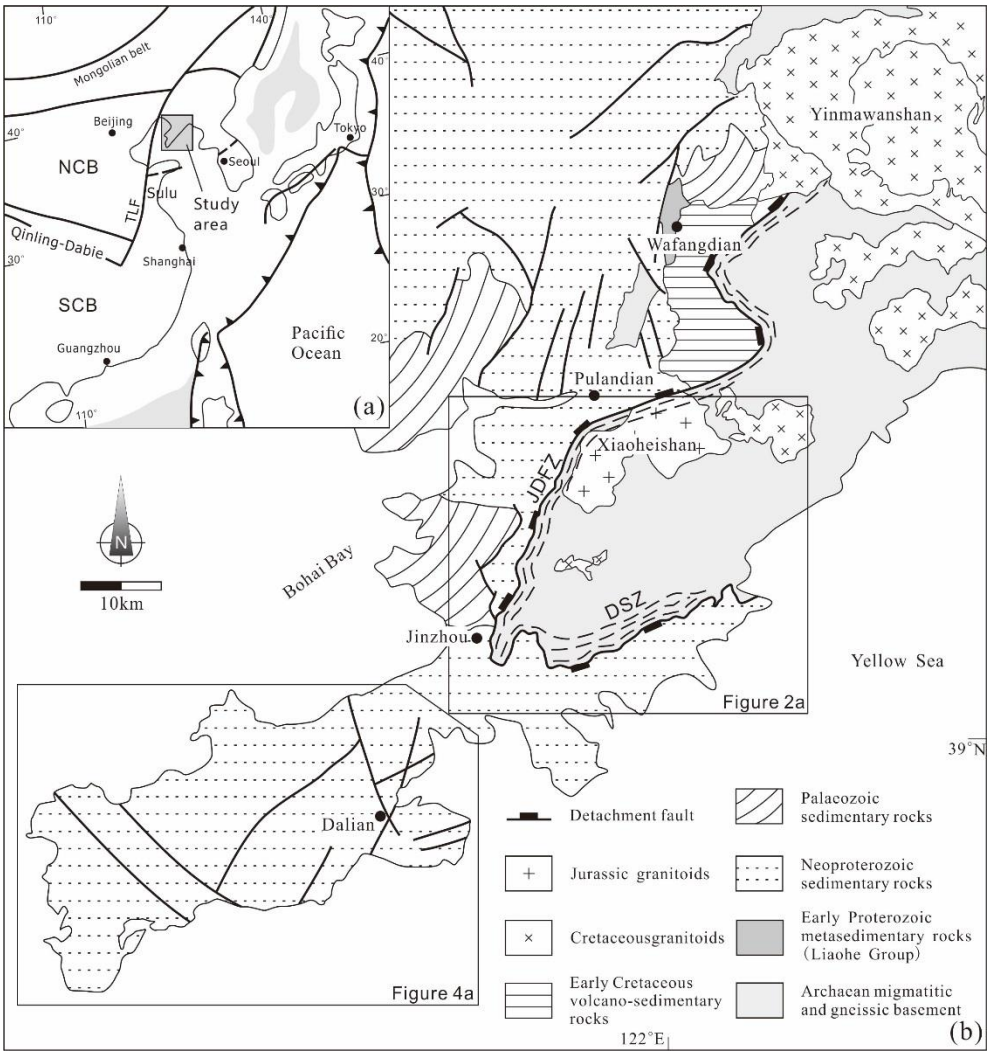

Figure1. (a) Structural outline of the eastern part of eastern China. (b) Structural geology of the Liaonan MCC.

2. Geological Overview

Studies on the Liaonan MCC dated back to 1980's when Yang et al. (1985) described the DSZ as an Archean ductile shear zone. Cui et al. (1986) first proposed that there is a Mesozoic detachment between the Archean basement and the sedimentary cover in southern Liaoning. Xu et al. (1991) argued that the southern Liaoning has a typical thin-skinned crustal structure due to contractional deformation, similar to the "thrusting-granite intrusion-ductile low angle normal fault" in French Central Massif, but different from the MCC's in the western Cordilleran. Hong et al. (1994) first proposed that the southern Liaoning region is an MCC structure formed under extension, which is subsequently studied in detail as a Triassic MCC by Yang et al. (1996). Liu et al. (2005) suggested that the Liaonan MCC is a typical Cordilleran type MCC that has one arc-traced detachment fault zone comprised by the JDFZ on

the western part (NW dip) and the DSZ on the southern part (SE dip). In their model, the JDFZ and DSZ form one single detachment fault zone. The exhumation of the MCC was attributed to early Cretaceous regional tectonic extension, which was later constrained between 121Ma and 113Ma by Yang et al. (2007, 2008) applying $^{40}Ar/^{39}Ar$ thermochronology studies of ductily sheared rocks along the JDFZ.

The Liaonan MCC consists of three major elements, i.e., a master detachment fault zone, an upper plate and a lower plate (Figure 2a). The lower plate contains the TTG igneous suite and supracrustal rocks of amphibolite facies that are dated as Archean protoliths (Liu et al., 2006) which are intruded by early Cretaceous syn-extensional granites. The upper plate is mainly composed of an early Cretaceous supradetachment basin sitting on Neoproterozoic to Paleozoic sedimentary rocks. The basin is normal fault-bounded and filled with early Cretaceous volcanic-sedimentary rocks (Liu et al., 2013). The master detachment fault zone of the Liaonan MCC has two branches, i.e., the Jinzhou fault zone (JDFZ) striking NNE, and the Dongjiagou shear zone (DSZ) striking NEE (Figure 1b, Figure 2a; Liu et al., 2005; Ji et al, 2009). Their foliations dip to NW (JDFZ) and SE to S (DSZ), respectively. The detachment fault zone, lower plate metamorphic rocks and syn-kinematic granite plutons possess stretching lineations of identical orientations that are consistent with striations on the Jinzhou master detachment fault surface. The JDFZ has typical corrugation characteristics, and their hinges are generally parallel to the WNW-ESE oriented stretching lineations in underlying mylonites (Ji et al., 2009). Various shear sense indicators along both zones show consistent top-to-the-WNW shearing (Liu et al., 2005, 2011, 2013; Ji et al., 2009). Geochronological data from syn-kinematic granitic dikes from the JDFZ and intrusions from the lower plate constrain the shearing from 134 to 116 Ma (Guo, 2004; Wu et al., 2005a, b; Ji et al., 2009; Liu et al., 2013). The post-tectonic magmas were dated as 115Ma and 113Ma (Ji et al., 2009; Jiang et al., 2016). Based on the combination of the U-Pb and Ar-Ar ages, the lower plate of the Liaonan MCC was exhumed progressively and sequentially in two different stages (an early, slow exhumation and a late, rapid exhumation) during crustal extension (Liu et al., 2013).

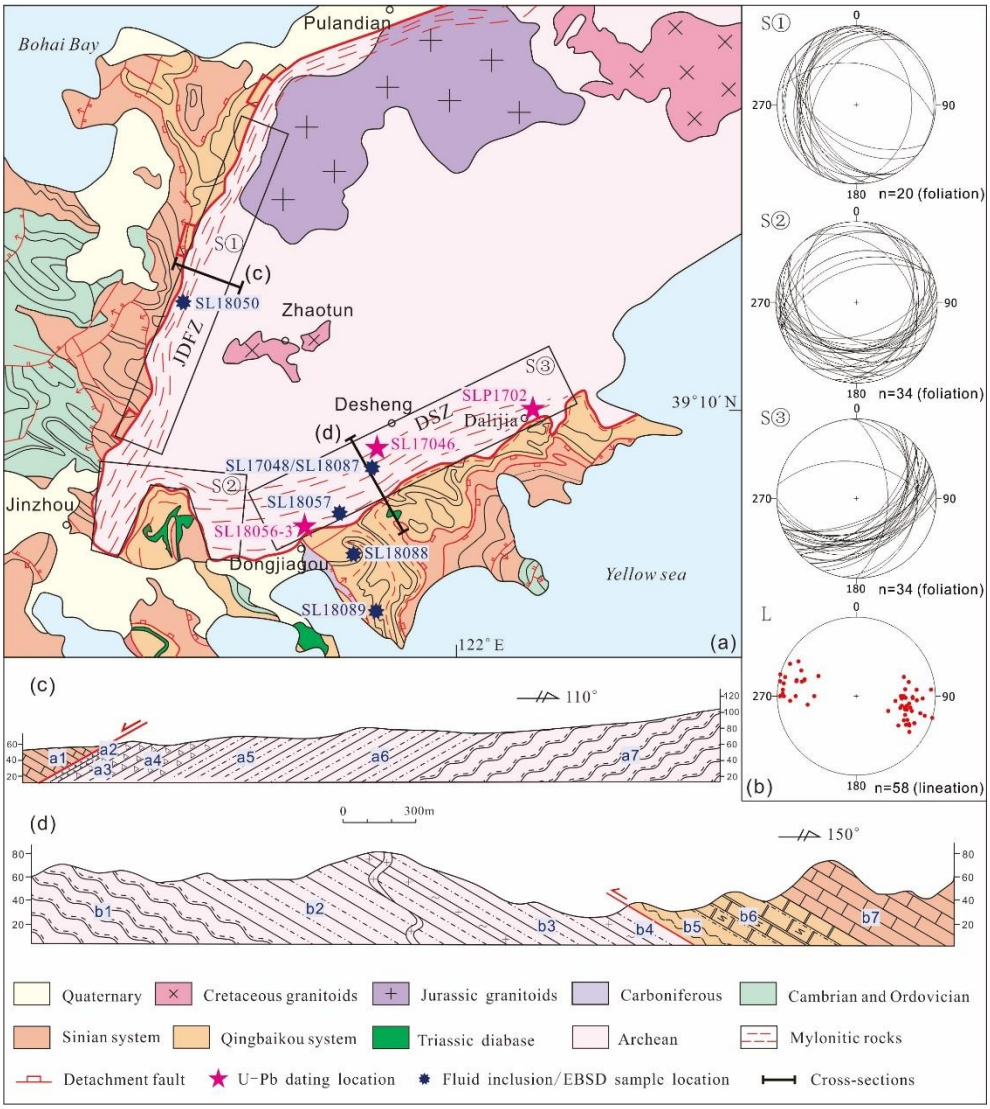

Figure 2. (a) Geological map of Liaonan MCC. (b) Stereoplots of foliations and stretching lineations for field areas S1, S2 and S3 (see boxes on map). (c) Typical cross-section of the JDFZ. (d) Typical cross-section of the DSZ. c_1. Mylonitic gneiss. c_2. Mylonites. c_3. Chloritic microbreccias. c_4. Brecciated mylonites. c_5. Fault gouges with local occurrence of pseudotchylites. c_6. Undeformed limestone. d_l. Gneiss. d_2. Mylonites. d_3. Phyllonite. d_4. Sheared muscovite schist and phyllite. d_5. Deformed quartzite and marble. d_6. Undeformed limestone.

3 Deformation structures of the Liaonan MCC

Deformation of the 2 structural units, i.e., the JDFZ and DSZ, characterize the structural evolution of the Liaonan MCC. Some sub-dome structures in the upper plate of the DSZ in southern Liaonan show similar structural characteristics and kinematics to the above structural units and may also provide important information on the exhumation of the Liaonan MCC.

3.1 JDFZ

The JDFZ is the western branch of the Liaonan MCC. The most significant

feature of the JDFZ is the occurrence of a thick sequence of fault-related rocks that record the detachment faulting at different crustal levels (Liu et al., 2005, 2013, 2016; Ji et al., 2015). From a typical cross-section across the JDFZ (Figure 2c), fault rocks include, from the lower plate to the master detachment fault, gneisses (Figure 2c_1), mylonites (Figure 2c_2), cholritic microbreccias (Figure 2c_3), brecciated mylonites (Figure 2c_4), fault gouges and pseudotchylites (Figure 2c_5).

3.1.1 The mylonite zone

The mylonite zone is about 1.5 km thick, which is constituted by macroscopic banded or augen structures. Feldspar porphyroblasts in generally fine-grained matrix have rotated and stretched tails of quartz grains. Quartz grains in the mylonites across the JDFZ show transitional characteristics from grain boundary migtation (GBM), subgrain rotation recrystallization (SGR) to bulging dynamic recrystallization (BLG), coupling with their c-axis fabrics from X-axis to Y-axis and Z-axis maxima, respectively (Liu et al., 2016). These characteristics are evidence for plastic deformation of quartz from high to low temperatures, or from amphibolite facies to greenschist facies, which imply that the lower plate rocks experienced exhumation from the middle-lower crust (Liu et al., 2005, 2013, 2016; Shen; 2010; Charles et al., 2012; Ji et al., 2015).

The mylonites where the sample SL18050 was taken along the JDFZ (Figure 2a) are characterized by progressive shearing in the following sequences: (1) The formation of mylonitic foliations accompanying emplacement of early granitic dikes, and formation of boudinage structures (Figure 3a); (2) progressive mylonitization inducing S-C (Figure 3b) and C’ fabrics; (3) as well as superimposed folding at the necking position of the dike (Figure 3a); (4) The emplacement of granitic dike that were relatively weakly sheared (Figure 3c). Mylonitic foliations and early folds are truncated by the dikes.

Various structural patterns, e.g., shear bands in banded mylonites (Figure 3d), rotated blocks of mylonitic gneisses (Figure 3e), and asymmetrical tectonic lenses, indicate the top-to-the-WNW shearing along the JDFZ. Different from the banded mylonites, the blocks and lenses are relatively massive and blocky with penetrative mylonitic foliations, which record higher temperature shearing in an early stage.

3.1.2 The sedimentary rocks in the upper plate

The upper plate consists of Neoproterozoic to lower Paleozoic sedimentary rocks, which are mainly non- or weakly-deformed limestones and quartz sandstones (Figure 3f). The bedding of the sedimentary rocks in the upper plate dips predominantly to the ENE (Figure 2c_6), which is opposite to dipping directions of foliations in the mylonites of the lower plate. Some sedimentary layers in the hanging wall is folded when approaching the master detachment fault surface, which also indicates top-to-the-WNW shearing along the master fault.

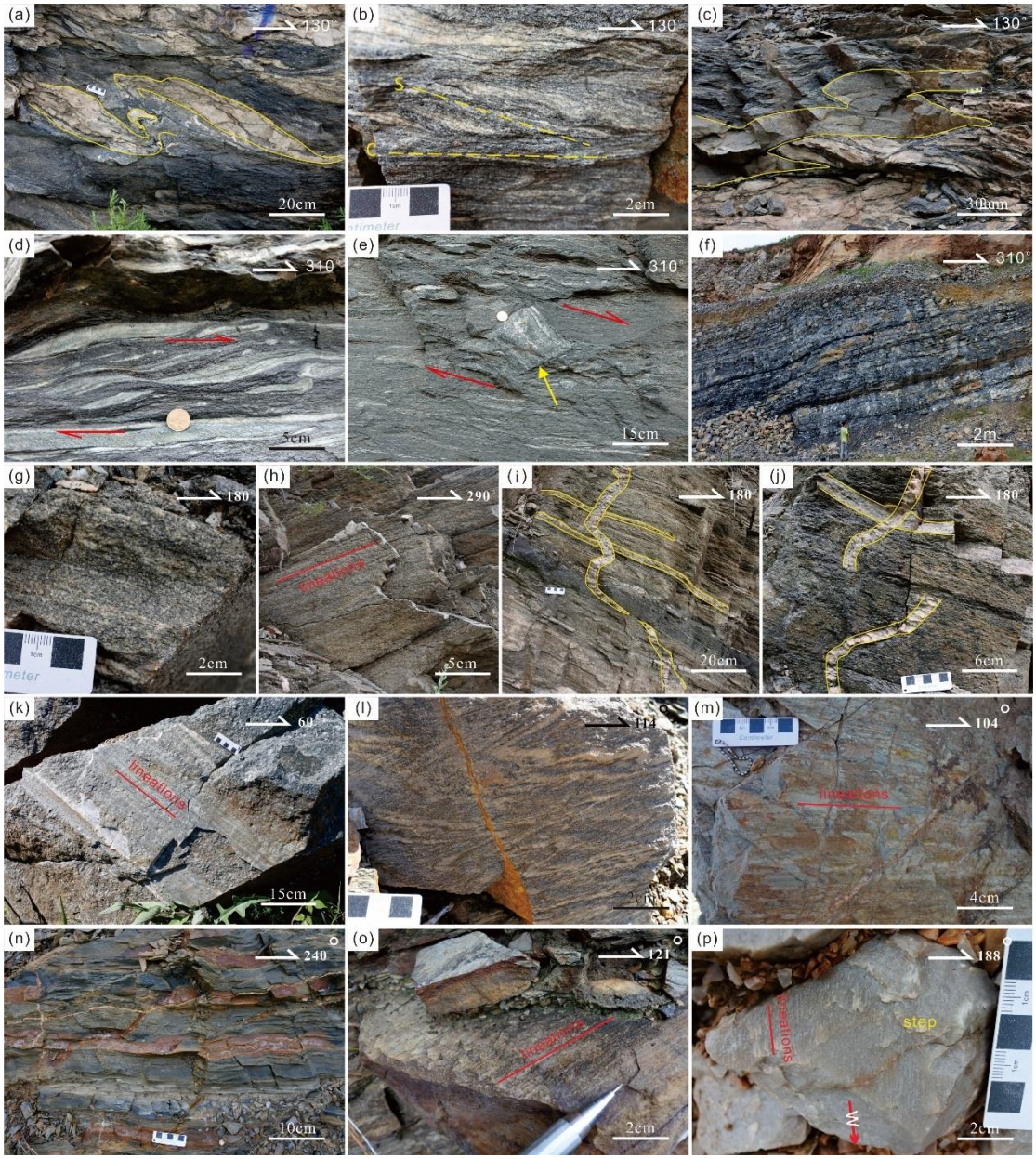

Figure 3. Outcrop structures of sheared rocks in the JDFZ (a-f), DSZ (g-m) and sub-domes (n-p).

(a) Progressive shearing after early boudinage of granite veins. (b) S-C fabrics. (c). Late diorite vein crosscut the foliations. (d) Small scale shear band indicating the top-to-the-WNW shearing. (e) Shearing inclusion of early stage. (f) Undeformed limestones. (g) Penetrative feldspar of fish shape. (h) Foliations and Lineations. (i) Multiple dike intrusions. (j) Sliding surface crosscut the granitic dike. (k) Lineations developed in the interface of quartz vein and mylonite. (l) Folding in banded marble. (m) Discrete foliations and lineations. (n) Quartz sandstone. (o) Lineations in slate (290°∠3°). (p) Lineations and steps in quartzite.

3.2 DSZ

The DSZ is the southern branch of the Liaonan MCC, which consists of two major tectonic units, i.e., Lower Unit of Archean gneisses and Upper Unit of

Neoproterozoic meta-sedimentary rocks (Figure 2d). The two Units are separated by a tectonic discontinuity contact (TDC, Chen et al., 2016). Rocks from both units have significant metamorphic differences, but they have consistent structural elements (lineations, foliations and kinematics).

3.2.1 Lower Unit

The Lower Unit mainly consists of Archean gneisses, being identical to the lower plate of the JDFZ. Rocks from the Lower Unit are granitic mylonites transiting to biotite plagioclase gneisses from near the contact to the central part of the lower plate. The granitic mylonites near the contact are banded, and have strong foliations and lineations. Feldspar grains form augens of aggregates that have subrounded shapes. Trailing tails of the augens are indicative of top-to-the-WNW shearing. The biotite plagioclase gneisses at the central part of the lower plate have subrounded feldspar grains or form feldspar fishes due to high temperature shearing.

Rocks from the Lower Unit experienced progressive shearing, shown by the deformation structures and microstructures of rocks. Biotite plagioclase gneisses located at SL18087 (Figure 2a) show the following sequences: (1) Widespread feldspar fishes formed in the early mylonitization (Figure 3g) indicate a relatively high temperature at early shearing; (2) Foliations and lineations are developed due to mylonitization of early granitic veins and gneisses (Figure 3h); (3) Granitic dikes that crosscut the mylonitic foliations suffer weak shearing. They are weakly folded (Figure 3i); (4) Localized mica-rich sliding surfaces with striation crosscut early granitic dikes (Figure 3j).

The granitic mylonite located in SL18057 (Figure 2a) possess characteristics of progressive deformation in the following sequences: (1) Early stage medium-high temperature mylonitization indicated by feldspar augens or subrounded porphyroclasts; (2) Late stage low temperature simple shearing shown by intensive deformation of quartz veins that are parallel to the foliations. Lineations are developed along the contacts with their surrounding mylonites (Figure 3k).

3.2.2 Upper Unit

The Upper Unit consists of metamorphosed Neoproterozoic to lower Paleozoic sedimentary rocks, e.g., phyllonite, mica schist, metamorphic quartz sandstone, calcareous slate, etc. Shearing foliations are paralleling to their primary sedimentary beddings. The planar fabrics (bedding and foliations) dip predominantly to the SSE near the TDC, which is consistent with the Lower Unit (Figure 2d). Progressive shearing was also developed in rocks from the Upper Unit, which is shown as: (1) The development of intrafolia folds in banded marbles (Figure 3l); (2) Stretching lineations on the discrete foliations by late shearing (Figure 3m).

3.3 Sub-domes in southern Liaonan

Away from the TDC at the upper plate of the DSZ, Neoproterozoic rocks (including Diaoyutai (Qnd), Nanfen (Qnn) and Qiaotou (Qnq) Formation of Qingbaikou System, and Changlingzi (Zc), Nanguanling (Zn), Ganjingzi (Zg) and

Yingchengzi (Zy) Formation of Sinian System; Figure 4a) have foliations with various dipping directions and low dip angles, forming several sub-domes. Archean gneisses are not exposed in the area. Quartz sandstone (Figure 3n), slate (Figure 3o) and quartzite (Figure 3p) of Qingbaikou System have well-developed foliations and stretching lineations, and show lens-shaped structures. Although the foliations dip to various directions in the dome-shaped structures, the stretching lineations also striking to WNW-ESE (Figure 4b). Shear sense indicators are compatible at different places with top-to-the-WNW shearing (Figure 3o and 3p), which is consistent with the JDFZ and DSZ.

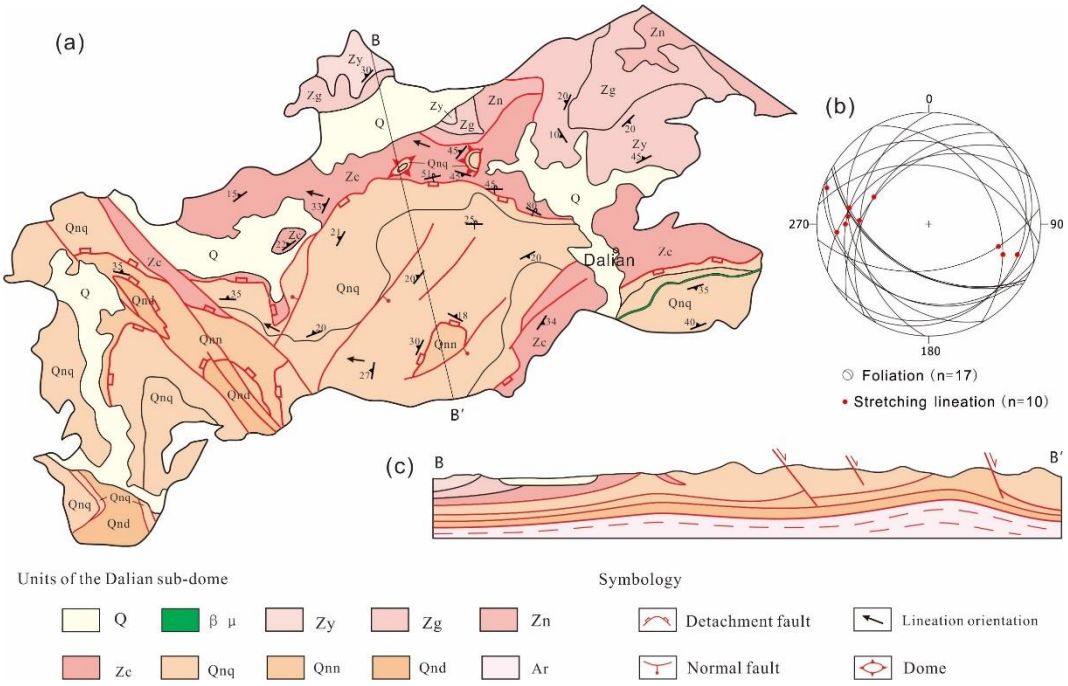

Figure 4. (a) Geological map of sub-domes in southern Liaonan. (b) Stereoplot of foliations and stretching lineations. (c) Cross-section of the sub-dome.

4 Methods and sampling strategy

Much work has been conducted along the JDFZ in previous studies, but the role of the DSZ in the formation of Liaonan MCC has been neglected. To clarify the detailed structure characteristics and constrain the tectonic evolution of DSZ, we took a series of samples from different structural horizons along the DSZ (Figure 2), and the following experimental approaches have been completed.

4.1 Methods

4.1.1 Thermometric analysis and Laser Raman Spectrum of fluid inclusions

Doubly polished thin sections (b0.30 mm thick) were made, and fluid inclusions were carefully observed to identify their genetic and compositional types, spatial clustering. Microthermometric measurements were performed using the Linkam THMSG600 heating-freezing stage and employing standard procedures in the institute of Mineral Resources, Chinese Academy of Geological Sciences. The estimated

precision of the measurements is ±0.1 °C for temperatures lower than 30 °C; and ±1 °C for temperatures higher than 30 °C. Salinities, densities and temperatures of inclusions were calculated using the ice points (Bodnar, 1983; Bischoff, 1991). Densities of the inclusions were calculated using the Flincor procedure (Brown, 1989). The temperatures were calibrated using the P-T diagram proposed by Lu et al. (1990). In the experiment, the primary inclusions were selected to calculate the temperatures, while the secondary inclusions were strictly removed.

Compositions of inclusions were identified using Laser Raman spectroscopy in the institute of Mineral Resources, Chinese Academy of Geological Sciences. An argon laser with a wave length of 514.53 nm was used as laser source at a power of 20 mW. The spectral resolution is 1~2cm^{-1} with a beam size of 1 μm. The scanning range is 100~4500cm^{-1}. Instrumental setting was kept constant during all analyses. The representative fluid inclusions with different types were selected for Raman analysis. The results of Raman analysis are shown in Figure 8.

4.1.2 EBSD analysis

The crystallographic preferred orientation (CPO) of quartz, especially the study of quartz c-axis fabric, is widely used in structural geology, such as defining deformation temperature, determining shear direction, and analyzing deformation history. XZ sections (paralleling to lineation and normal to foliation) were cut from the samples and polished using Buehler Mastermet colloidal silica and Buehler grinderpolisher. The LPO data acquisition was finished on a Hitachi S-3400 N-II scanning electron microscope mounted with Nordlys EBSD Model NL-II detector with the thin section surface inclined at 70° to the incidental beam. The new technique can provide fast data acquisition of mineral grains or part of mineral grains of interest, with 0.1 μm spatial resolution and 0.5° angular resolution. Acceleration voltage of 15 kV is applied, and working distance is 18.4mm. EBSP analysis is finished using the HKL Channel 5 software package. All the EBSD analysis was finished in the State Key Laboratory of Geological Processes and Mineral Resources, China University of Geosciences (Beijing).

4.1.3 LA-ICP-MS dating

Zircon grains were separated from whole-rock samples using conventional techniques. After crushing and sieving of the samples, heavy minerals were concentrated by panning and magnetic separation. Zircon grains were mounted in epoxy and carefully polished until their cores were exposed. Cathodoluminescence (CL) images of zircons combined with reflected and transmitted light images were used for analyses. U-Pb dating analyses of zircon were conducted at the Laser Ablation Inductively Coupled Plasma Mass Spectrometry (LA-ICP-MS) microanalysis laboratory, affiliated to the State Key Laboratory of Geological Processes and Mineral Resources, China University of Geosciences, Beijing. Laser sampling was performed using a Coherent's GeoLasPro-193nm system. A Thermo Fisher's X-Series 2 ICP-MS instrument was used to acquire ion-signal intensities. Helium was applied as a carrier gas. Argon was used as the make-up gas and mixed

with the carrier gas. All data were acquired on zircon in single spot ablation mode at a spot size of 32 μm with 6 Hz frequency in this study. Zircon 91500 was used as an external standard for U-Th-Pb isotopic ratios (1065Ma, 2.5Ma, 0.9Ma; Wiedenbeck et al., 1995, 2004). Meanwhile zircon Mud Tank was used as a monitoring standard for each analysis (Black & Gulson, 1978). Time-dependent drifts of U-Th-Pb isotopic ratios were corrected using a linear interpolation (with time) for every five analyses according to the variations of 91500. Each analysis incorporated a background acquisition of approximately 20s (gas blank) followed by 50s data acquisition from the sample. Off-line selection and integration of background and analyte signals, and time-drift correction and quantitative calibration for trace element analyses and U-Pb dating were performed by ICPMSDataCal (Liu et al., 2008). Data reduction and concordia plotting diagram was carried out using the Isoplot 4.5 (Ludwig, 2008).

4.2 Sampling strategy

4.2.1 Samples of fluid inclusion studies and EBSD analysis

The selected samples are all collected from the DSZ (Figure 2).

Samples SL17048, SL18057, SL18088, SL18089 are syn-tectonic quartz veins taken from different structural horizons (Figure 2a) for fluid inclusion temperature measurement and laser Raman testing. The sample SL17048 from the lower plate have quartz grains with extensive grain boundary migration recrystallization (Figure 5a). Quartz grains in the sample SL18057 from mylonites at the lower plate near the TDC are distributed in a stripped grain aggregate. The small new grains are characteric of subgrain rotation recrystallization (Figure 5b). Bulging dynamic recrystallization is the major mechanism of grain size reduction in the sample SL18088 and SL18089 from the mylonized upper plate rocks (Figure 5c). Some coarse grains in the sample SL18089 exhibit weak undulose extinction.

Samples SL18087-5/-6, SL18057-1/-2, SL18088-2/-3 were collected from different structural horizons (Figure 2a) for EBSD analysis. Samples SL18087-5/-6 are mylonitic gneisses from the lower plate, which show the dispersive lens-shaped feldspar (SL18087-5, Figure 5e) and connected biotite grains along foliations (SL18087-6, Figure 5f). Samples SL18057-1/-2 are quartz vein paralleled to foliations with quartz grains possess subgrain rotation recrystallization (Figure 5b) and wall rock of mylonitic granitic mylonite with muscovite grains connected to be foliations, respectively. Samples SL18088-2/-3 are banded marbles located in the Upper Unit, showing C’ fabrics (Figure 5g) and well-developed S-C' fabrics (Figure 5h).

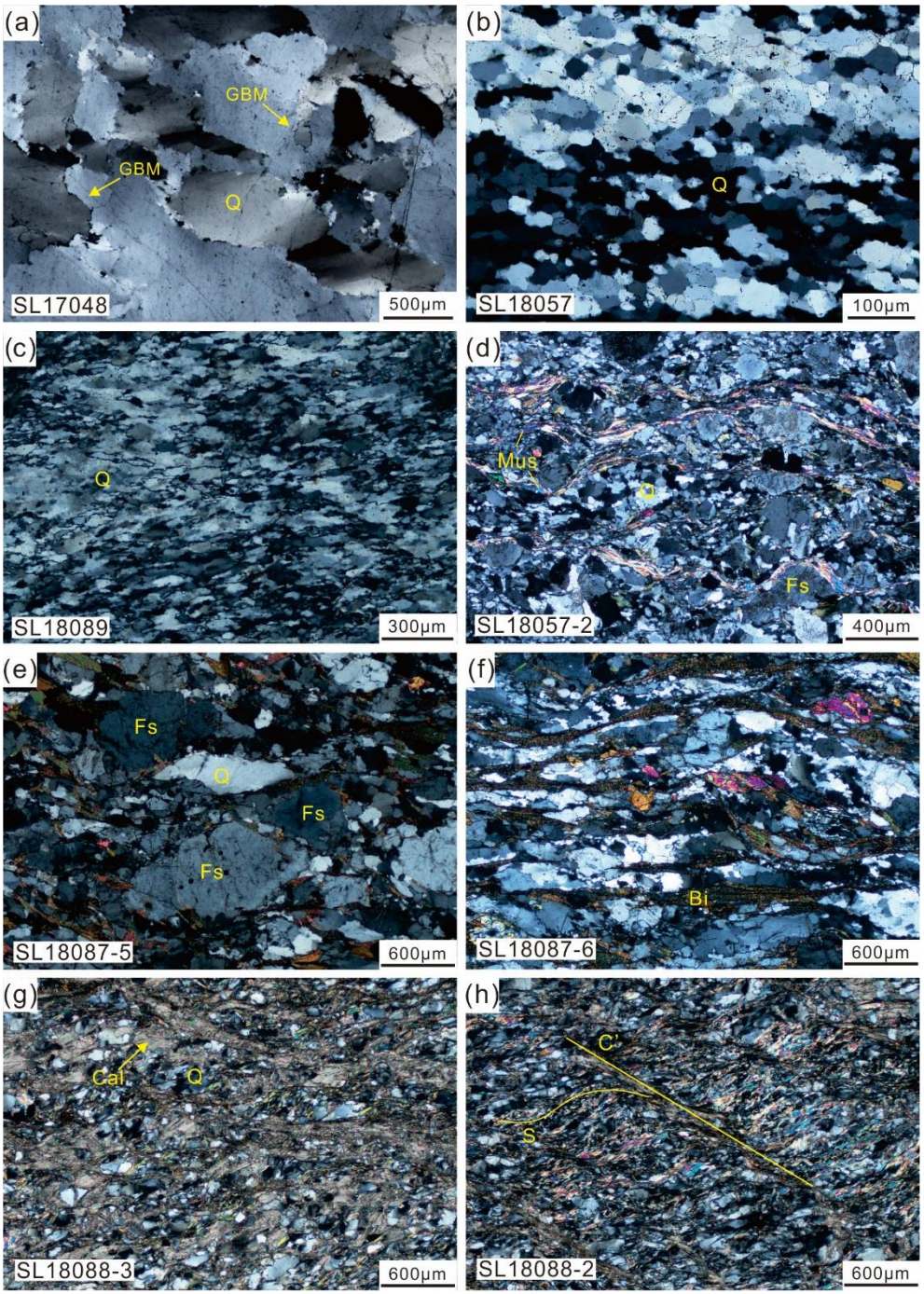

Figure 5. Microphotos showing mineral components and microstructures of rocks along the DSZ.

(a) Grain boundary migration of quartz in Sample SL17048. (b) Subgrain rotation recrystallization of quartz. (c) Banded and bulging dynamic recrystallization of quartz. (d) Feldspar porphyroblasts and muscovite grains with parallel arrangement. (e) Dispersive lens-shaped feldspar and quartz grains. (f) Connected biotite grains along foliations. (g) C' fabrics in a sheared calcareous siltstone. (h) S and C' fabric in phyllonite.

4.2.2 Geochronology samples

Three granitoid samples of syn-kinematic dikes from the DSZ were selected for zircon U-Pb dating. The granitoids were emplaced into the mylonites of the Lower Unit and experienced the shearing event. The geochronological data of these dikes with different structural characteristics become essential to constrain the timing relations of JDFZ and DSZ. Sample locations are shown in Figure 2a and Figure 6.

Sample SL18056-3 (39º5′0.5″N, 121º51′46.7″E) was collected from Dongjiagou Town. The sample is the late stage one of the two syn-kinematic granite dikes (Figure 6), showing truncation relationships with the early dike and possessing mylonitic characteristics along the margins. The sample is a medium-grained, light gray mylonitized granite that consists mainly of plagioclase (40-50%), K-feldspar (10-15%), quartz (25-30%) and a minor amount of mica. Serrated quartz grain boundaries indicate high-temperature grain boundary migration recrystallization. Euhedral of feldspar and grain boundary migration of quartz suggest high-temperature deformation.

Sample SLP1702 (39º9′46.6″N, 122º3′35.8″E) was collected from Dalijia Village, which is a folded light-gray granitic dike intruded into mylonite. The hinge of the fold is nearly parallel to the lineations, indicating the characteristics of A-type fold. Foliations were cut by the dike but they are continuous in the mylonites in the hinge area, which is an important evidence of syn-kinematic dike (Figure 6). This sample is a fine-grained mylonitized granite that consists mainly of K-feldspar (20-25%), plagioclase (25-30%), quartz (30-35%), biotite (5%), and chlorite (3%). Quartz grains have been strongly deformed into ribbons that have largely recrystallized into smaller grains through subgrain rotation recrystallization. The long axes of the grains are parallel to the foliation (Figure 6).

Sample SL17046 (39º8′45.9″N, 121º56′7.2″E) was collected from Desheng Town, which expresses the irregular shape in the field. Part of the granitic dike developed in parallel to the foliations, while other parts cut off the foliations. This sample is a medium-grained, light-gray mylonitized granite invaded into the gneiss, which consists mainly of K-feldspar (30-40%), plagioclase (10-15%), quartz (30-40%), and biotite (~10%). Intragranular fractures in remnant feldspar crystals and the sub-granular shapes of lobate quartz grains indicate a subsequent low-temperature deformation event (Figure 6).

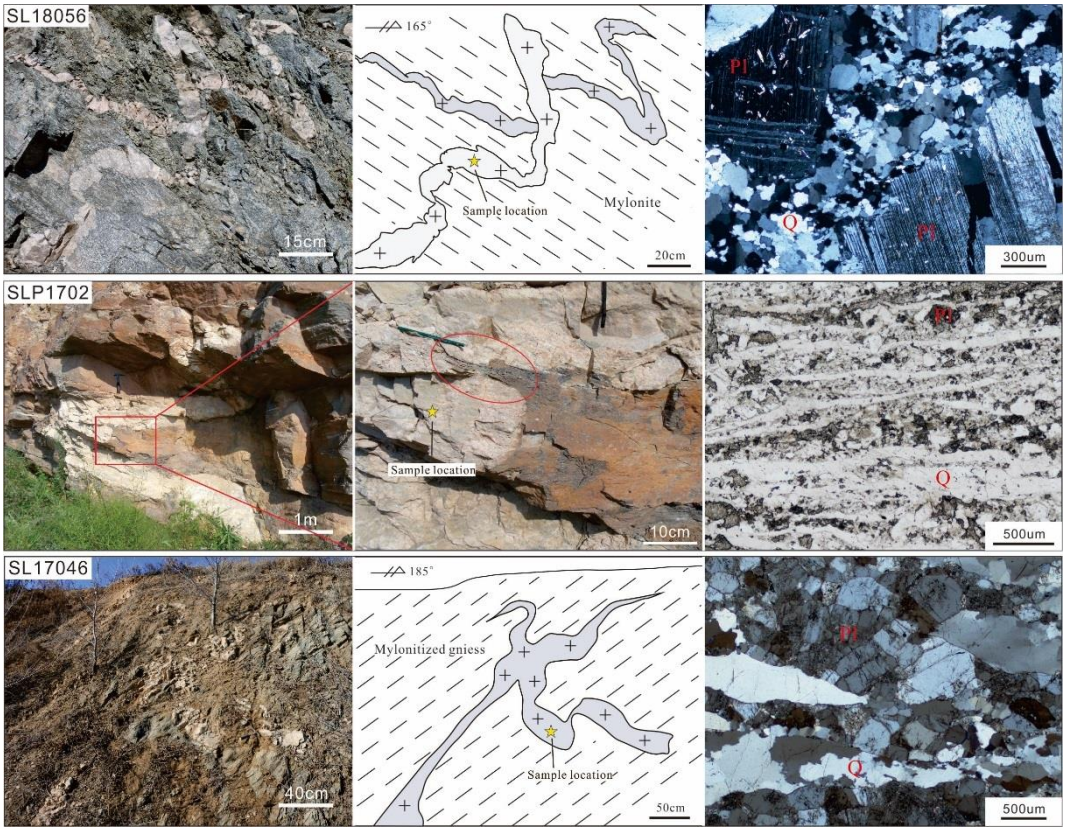

Figure 6. Outcrops and microscopic structures of the dated granite samples.

5 Results

5.1 Thermometric analysis and Laser Raman Spectrum of fluid inclusions

Primary inclusions have irregular shapes, such as elliptical or fusiform, ranging in sizes of 2-20μm. Most have sizes from 4 to10μm. There are two types of inclusions in the quartz vein. One is two-phase inclusions of gas and liquid, which account for more than 90% of the inclusions. They are isolated or distributed in small groups (Figure 7a-d). The other is three-phase inclusions containing CO_2, with a distinct "double eyelid structure". They are only developed in syn-tectonic quartz veins from lower structural level (Sample SL17048; Figure 7e and 7f).

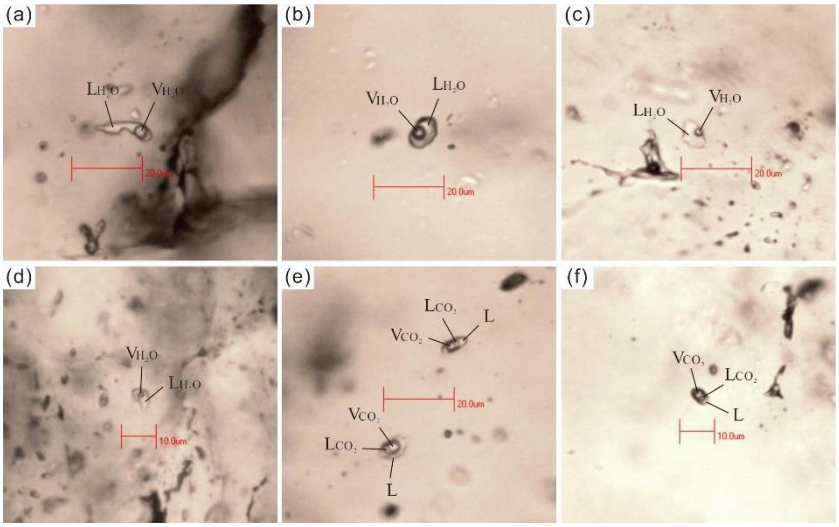

Figure 7. Microphotographs of fluid inclusions in quartz veins from the DSZ. (a-d) Primary two-phase inclusions. (e, f) Three-phase inclusion containing CO2.

Freezing point temperature (Tm) and homogenization temperature (Th) of more than 30 primary fluid inclusions are measured (Table 1). The salinity is calculated by the formula of Hall et al. (1988), as follows.

$$W_{NaCl}=0.00+1.78T_m-0.0442T_m^2+0.000557T_m^3.$$

The peak values are shown in Figure 8a, i.e., 185 °C (SL17048), 215 °C (SL18057), 225 °C (SL18088/SL18089). The measured freezing temperature and homogenization temperature, and the calculated salinity (Figure 8b) are calculated, according to the T-ρ phase diagram of the NaCl-H_2O system proposed by Bischoff et al. (1991), that the corresponding density is plotted (Table 1).

Table 1. Micro-thermometric data of fluid inclusions.

Sample Number	Mine-ral	Type of phase state	Proportion of phase state	Tm (°C)	Th (°C)	Salinity (wt%NaCleqv)	Density (g/cm^3)
SL17048	quartz	V+ L (V+LCO_2+L)	V=10~30 L CO_2=5~10 L=60~85	-12.4~-8.0	156.5~297.1	11.7~16.3	0.84~1.01
SL18057	quartz	V+L	V=10~20 L=80~90	-15.1~-9.5	153.8~337.1	13.4~18.7	0.84~1.04
SL18088	quartz	V+L	V=10~25 L=75~90	-4.8~-0.6	163.8~287.8	1.1~7.6	0.74~0.95
SL18089	quartz	V+L	V=8~15 L=85~95	-14.9~-10.6	147.2~230.1	14.6~18.6	0.83~0.97

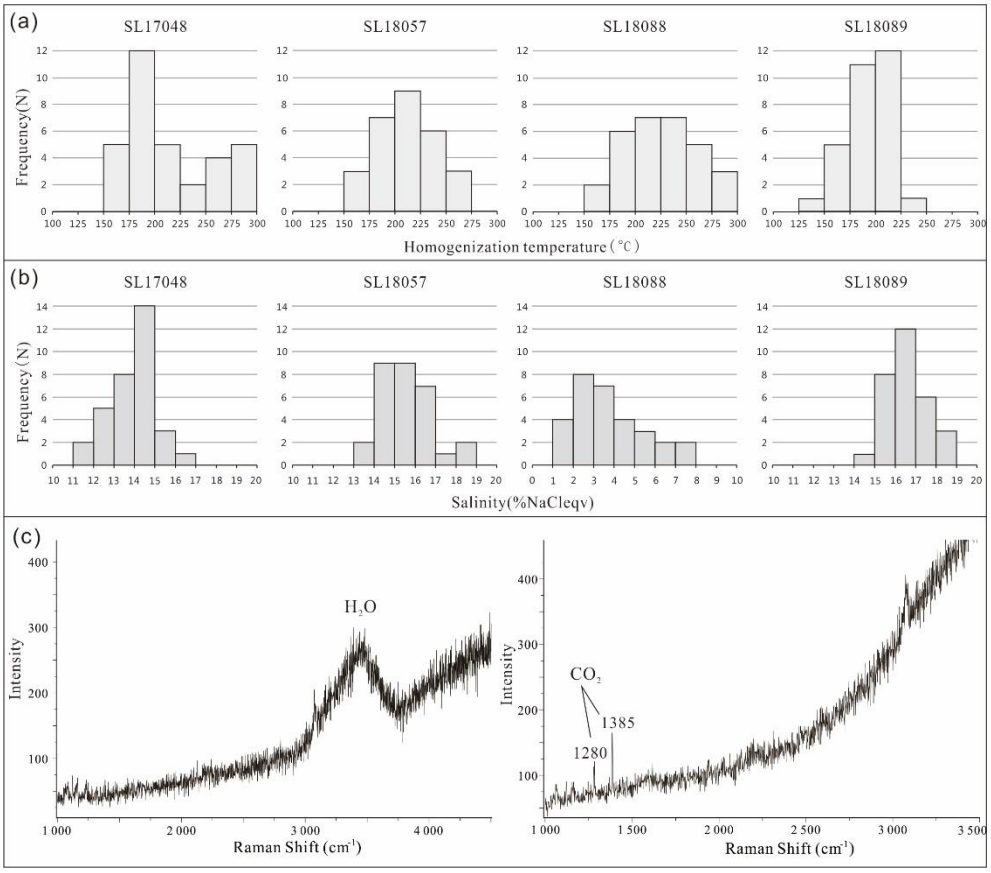

Figure 8. (a) Histogram of homogenization temperature. (b) Histogram of salinity. (c) Laser Raman spectrogram of fluid inclusions.

By using the P-T phase diagrams of different salinity in H_2O-NaCl systems proposed by Bodnar & Vityk (1994) and the fluid inclusion calculation software Flincor (Brown, 1989), we estimated the formation temperature and pressure of the measured quartz veins. The crystallization temperature and formation pressure of sample SL17048, SL18057 and SL18088/SL18089 is ca. 630 °C, 470 °C, 350 °C and about 700MPa, 420MPa, 200MPa, respectively. The results are consistent with those exhibited by their deformation microstructures. In addition, the depth of quartz vein formation is about 25 km (SL17048), 15 km (SL18057), 7 km (SL18088/SL18089) respectively (applying a density of ca. 2700 kg/m^3).

The liquid compositions in the liquid phase of the inclusions in most samples are mainly H_2O (peak 3310~3610 cm^{-1}; Figure 8c). Only the gas phase component of inclusions of the sample SL17048 has CO_2 (double peaks are 1285 and 1388 cm^{-1}; Figure 8c). This is consistent with the characteristics of fluid inclusions observed under the microscope. There are abundant CO_2-bearing three-phase inclusions in the sample SL17048 that was taken from the lowermost part of the DSZ near to the lower plate. The occurrence of CO_2 may be due to the large-scale magma activities that led to degasification of magmas (Liu et al., 2002).

5.2 Quartz c-axis fabrics

Point maxima or double-maxima superimposition are the dominant fabric patterns, which shows the structural superposition under the same tectonic stress field.

The fabrics of all samples indicate a history of progressive deformation from medium-high to low temperature (Stipp et al., 2002; Passchier & Trouw, 2005; Law, 2014).

Samples SL18087-5 and SL18087-6 are mylonitized gneiss, located at the bottom of DSZ. The c-axis fabric of SL18087-5 consists of a group of type I symmetrical maxima parallel to the Y-axis, and a type II symmetrical maxima located between the Z-axis and Y-axis, the maxima distributed independently as a point (Figure 9b). The type I symmetrical maxima parallel to the Y-axis is the result of the prism <a> slip at medium-high temperature condition (550-650 °C) which is consistent with the microstructure characteristic of quartz grain boundary migration recrystallization. The maxima located between the X-axis and the Y-axis is attributed to the rhomb <a> slip under the medium-low temperature (400-550 °C). The c-axis fabric of sample SL18087-6 maxima is along the Y_0 and Z_0 axis which indicates that low-temperature basal <a> slip superimposed on high temperature prism <c> slip (Figure 9a). It is consistent with the observation in the field that the relatively low temperature discrete foliations superimposed on the high temperature penetrative foliations.

Samples SL18057-1 and SL18057-2 are granitic mylonites, located at the top of the lower unit of DSZ. The c-axis fabric of SL18057-2 is composed of a combination of type I maxima and type I crossed girdle (Figure 9c). Type I maxima is composed of several point maxima groups which are not located along the Y axis, forming an irregular region. This kind of fabric is result from rhomb <a> slip at medium-low temperature condition (400-550 °C) or prism <a> slip at medium-high temperature condition (550-650 °C). This corresponds to mylonitization of the granite. The symmetry of type I crossed girdle is attributed to relatively large pure shear strain components, and the saturation of fabrics is limited by the magnitude of strain. The c-axis fabric of SL18057-1 shows maxima parallel to Y_0-axis, which is slightly extended along the Y_0Z_0 direction (Figure 9d). The asymmetry of the distribution and density of the maxima is good which indicates that the single shear deformation plays a dominant role. But at the same time, a relatively weak Z_0 maxima developed which indicates the superposition of simple shear deformation under the low temperature condition in the later stage. This also corresponds to the quartz vein intrusion in the later stage under relatively low temperature condition and the microstructure of the quartz vein expressing subgrain rotation recrystallization under the microscope.

Samples SL18088-2 and SL18088-3 are banded marbles, located at the upper unit of DSZ. The quartz c-axis fabric of SL18088-3 is a symmetrical type I crossed girdle consists of four type IV point maxima which is caused by rhomb <a> slip under medium-low temperature (400-550 °C, Figure 9e). The symmetrical type also indicates the deformation environment with relatively large pure shear component. This corresponds to the penetrating folding in the field. The quartz c-axis fabric of SL18088-2 and SL18088-3 is similar. Sample SL18088-2 also shows a Z_0 point maxima. The fabric is monoclinic symmetrical indicates that basal <a> slip at low temperature plays an important role and represents the superposition of simple shear deformation (Figure 9f).

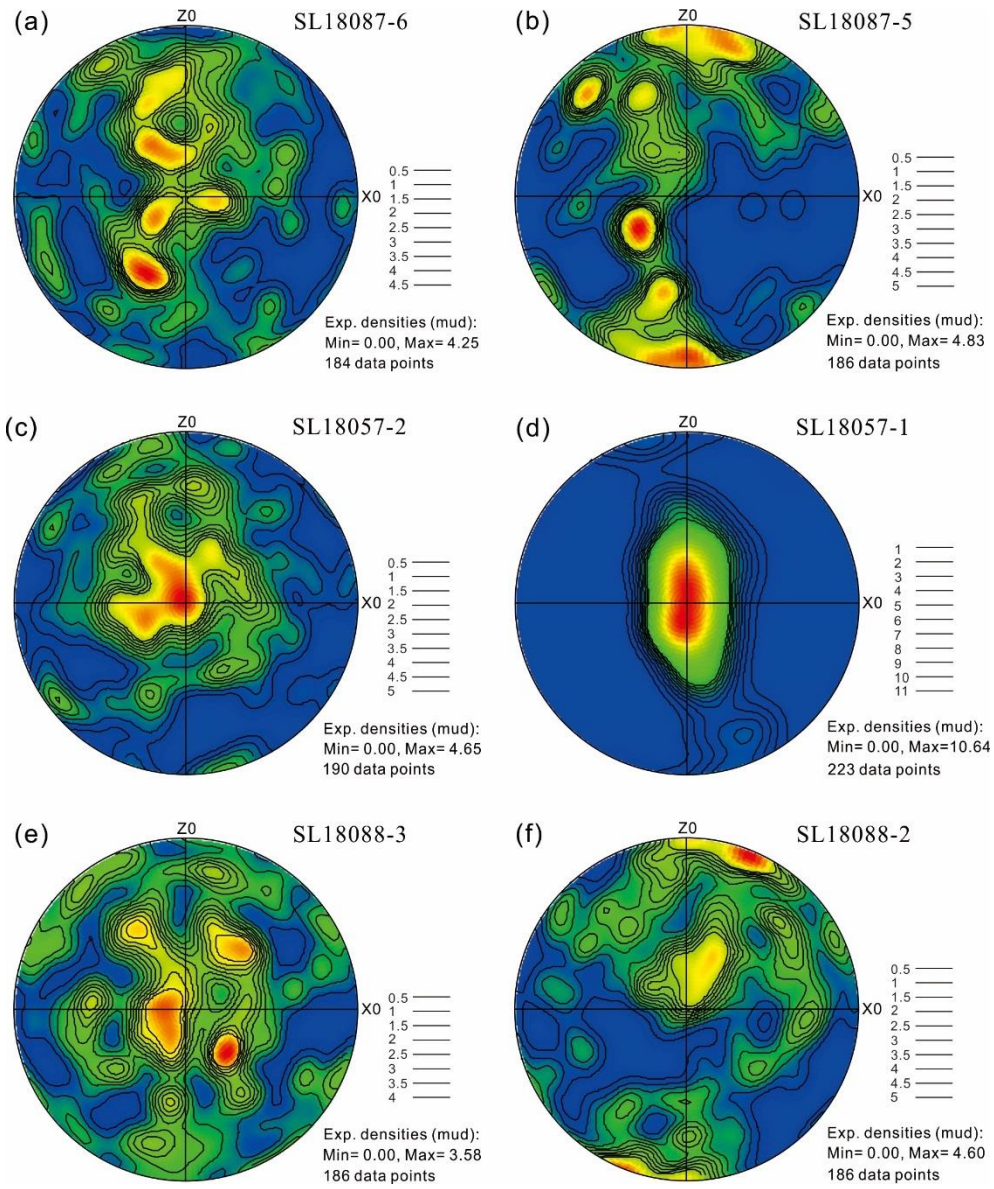

Figure 9. Quartz c-axis fabrics in the DSZ.

5.3 Geochronology of granitic dikes in the DSZ

Zircons in sample SL18056-3 are mainly colorless-light yellow, glassy luster, good transparent, mostly have euhedral grain shapes with long-short axis ratio of 1.2:1-3.3:1 and commonly 70-100 μm long (Figure 10a). In cathodoluminescence (CL) images, zircons show well-developed oscillatory zoning, indicating a magmatic origin. Some contain inherited relic cores and zircon grains are generally prismatic-rounded. At the margins, light-colored metamorphic edges are commonly less than 5 μm. Thirty-one U-Pb analyses were conducted for this sample and twenty-six effective analysis points were located on or near the concordia curve, and the weighted average age of $^{207}Pb/^{206}Pb$ was 2397±24 Ma (MSWD=0.77), and the zircons were judged to be magma-captured zircons (xenocrysts; Figure 10b).

Zircons in sample SLP1702 are commonly colorless, glass-grease luster, and have good transparency. They are euhedral shaped or long-columnar and

semi-cone-shaped. The grainsizes are 90-220 μm with long-short axis ratio of 1:1-3:1 (Figure 10c and 10e). In the CL image, zircons have various characteristics: (1) Some are typical magmatic zircons with well-developed oscillatory zoning; (2) The cores and edges of some magmatic zircons are obviously different, but all of them developed oscillatory zoning, which is formed by the superposition of multi-stage magmatic zircon growth; (3) Some are inherited zircons. There is oscillatory zoning in the margin but the core is cloudy; (4) The metamorphic zircons are more common and hydro-thermal dissolution structures are visible inside. Eighteen data points show nearly consistent group distribution, with a $^{207}Pb/^{206}Pb$ weighted average age of 2387±29 Ma (MSWD=0.35), which are the captured zircons (Figure 10c and 10d). Another eleven data points show nearly consistent group distribution, with a $^{206}Pb/^{238}U$ weighted average age of 138.3±1.6 Ma (MSWD=0.81), representing the age of the zircon crystallization from magma (Figure 10f).

Zircons in sample SL17046 are mainly colorless, transparent and columnar, with a length of 70-170 μm and long-short axis ratio of 1.2:1-4.5:1 (Figure 10g). In the CL image, zircon grains are tabular with no oscillatory zoning. Because of the serious lead loss, the weighted age has low concordance. Only 10 data points show a nearly consistent group distribution, with a $^{206}Pb/^{238}U$ weighted average age of 134.8±2.6 Ma (MSWD=0.59), which represents the age of emplacement of syn-kinematic dikes (Figure 10h).

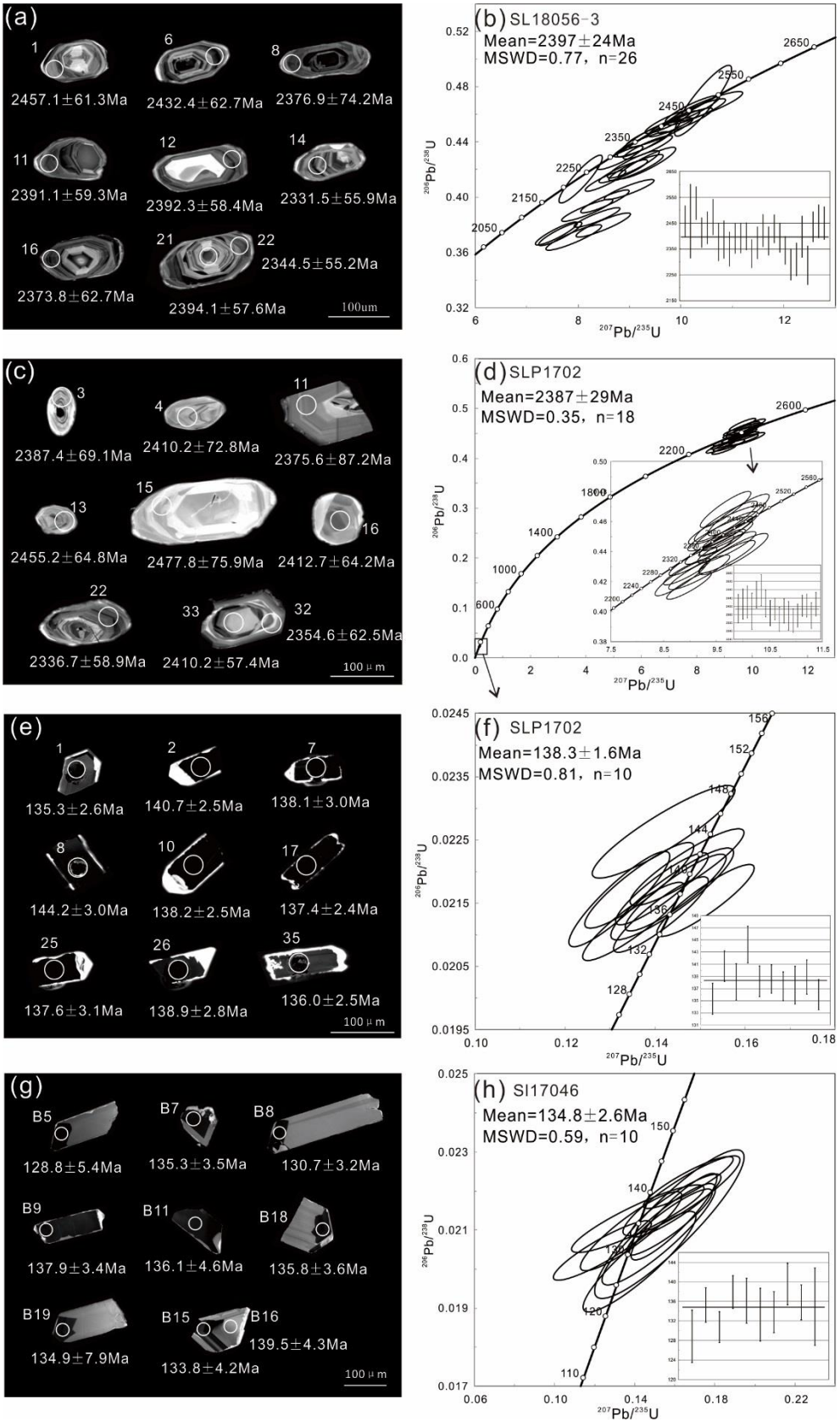

Figure 10. CL images of representative zircons (a, c, e, g) and zircon U-Pb concordia diagrams of the dated samples (b, d, f, h). Circles indicate spots and ages of the LA-ICPMS dating. MSWD = mean square weighted deviation; *n* = number of

analyzed spots.

6 Discussion

6.1 Contrasting deformation and structural evolution between JDFZ and DSZ

From similarities of orientations of stretching lineations (WNW-ESE) and kinematics (top-to-the-WNW) along both the JDFZ and DSZ, previous studies regarded them as a unified detachment fault zone (e.g., Liu et al., 2005; Ji et al., 2009; Ouyang et al., 2010; Li et al., 2012; Jiang et al., 2016). The results from the present studies, however, show that there are significant differences between the two structural systems.

The JDFZ and DSZ both consist of three components. As shown above, the JDFZ possesses characteristics of most detachment fault zones that typically have 1) a master detachment fault zone of a thick sequence of teconites from gneissic mylonites near the lower plate, to chloritic breccias and fault gauges near/along brittle rupture surface, 2) an upper plate of supradetachment basin sitting on non- or weakly deformed Neoproterozoic to lower Paleozoic sedimentary rocks, and 3) a lower plate of high-grade Archean gneisses metamorphosed up to lower amphibolite facies. In contrast, the DSZ is a large-scale shear zone encompassing 1) the Lower Unit of highly sheared Archean gneisses metamorphosed up to lower amphibolite facies, 2) the Upper Unit of metamorphosed Neoproterozoic to lower Paleozoic sedimentary rocks of up to lower greenschist facies, and 3) a major TDC between the lower and the upper units. An obvious metamorphic contrast exists across the TDC (Chen et al., 2016). However, rocks from both sides of the TDC possess structures and fabrics for identical shearing deformation that is consistent with shearing along the JDFZ. Comparing with the stratigraphic components of the DSZ, there is a loss of the bottom section of the Neoproterozoic strata, i.e., the Upper Unit ($Pt_3$1; Figure 11).

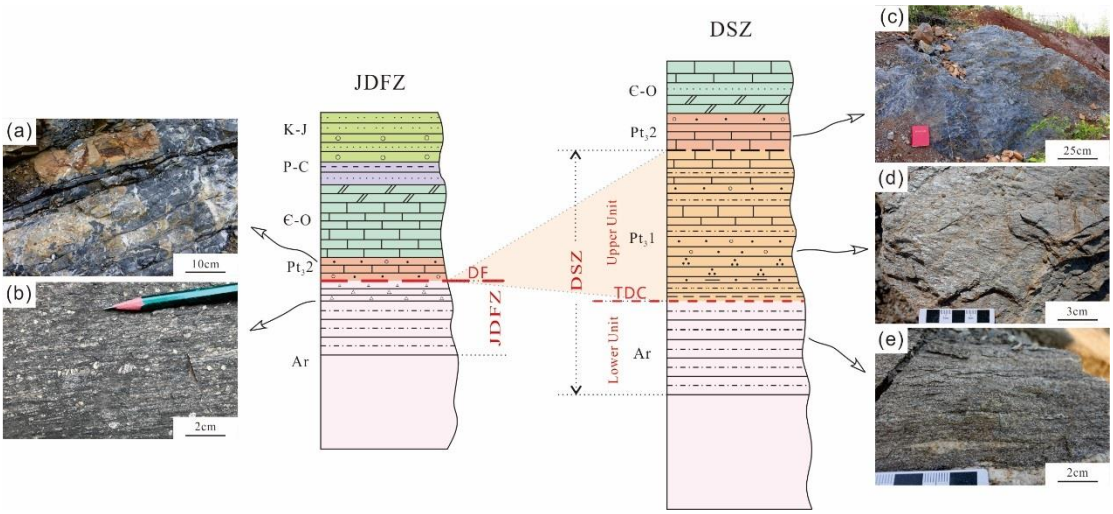

Figure 11. Stratigraphic columns of JDFZ and DSZ.
DF: detachment fault. TDC: tectonic discontinuity.

Macrostructure, microstructure and quartz c-axis fabrics all show significant progressive shearing both in JDFZ and DSZ, although different in deformation

characteristics. Tectonites from the JDFZ possess evidence for progressive exhumation of the lower plate from middle or lower crustal levels. Also, mylonites developed S-C fabrics and different types of syn-tectonic veins of JDFZ show the progressive mylonitization (SL18050; Figure 12a). Progressive deformation is also recorded in sheared rocks of different structural horizons from the DSZ. In the Lower Unit near the lower plate, biotite plagioclase gneisses (SL18087) with penetratively developed fish-shaped feldspar grains (indicating the relatively pure shearing) were superimposed by the discrete foliations and lineations. Striae were formed on the mica-rich surfaces possibly related to late shearing (Figure 12b). In the Lower Unit near the TDC, mylonitization in medium-temperature was dominated penetratively, superposed by quartz veins paralleled to foliations developing strong stretching lineations on the contact surface (Figure 12c). In the Upper Unit, intrafolial a-type folds were superimposed by foliations and lineations in deformed banded marbles (Figure 12d). The above discussions suggest that the rocks from the DSZ at different structural horizons experienced early high-temperature penetrative shearing and subsequent low-temperature shearing. It is also shown that both the JDFZ and DSZ experienced the early high-temperature penetrative shearing. The JDFZ was superimposed by the detachment faulting accompanying exhumation of the MCC, while continued progressive shearing at low temperatures was prevailing along the DSZ.

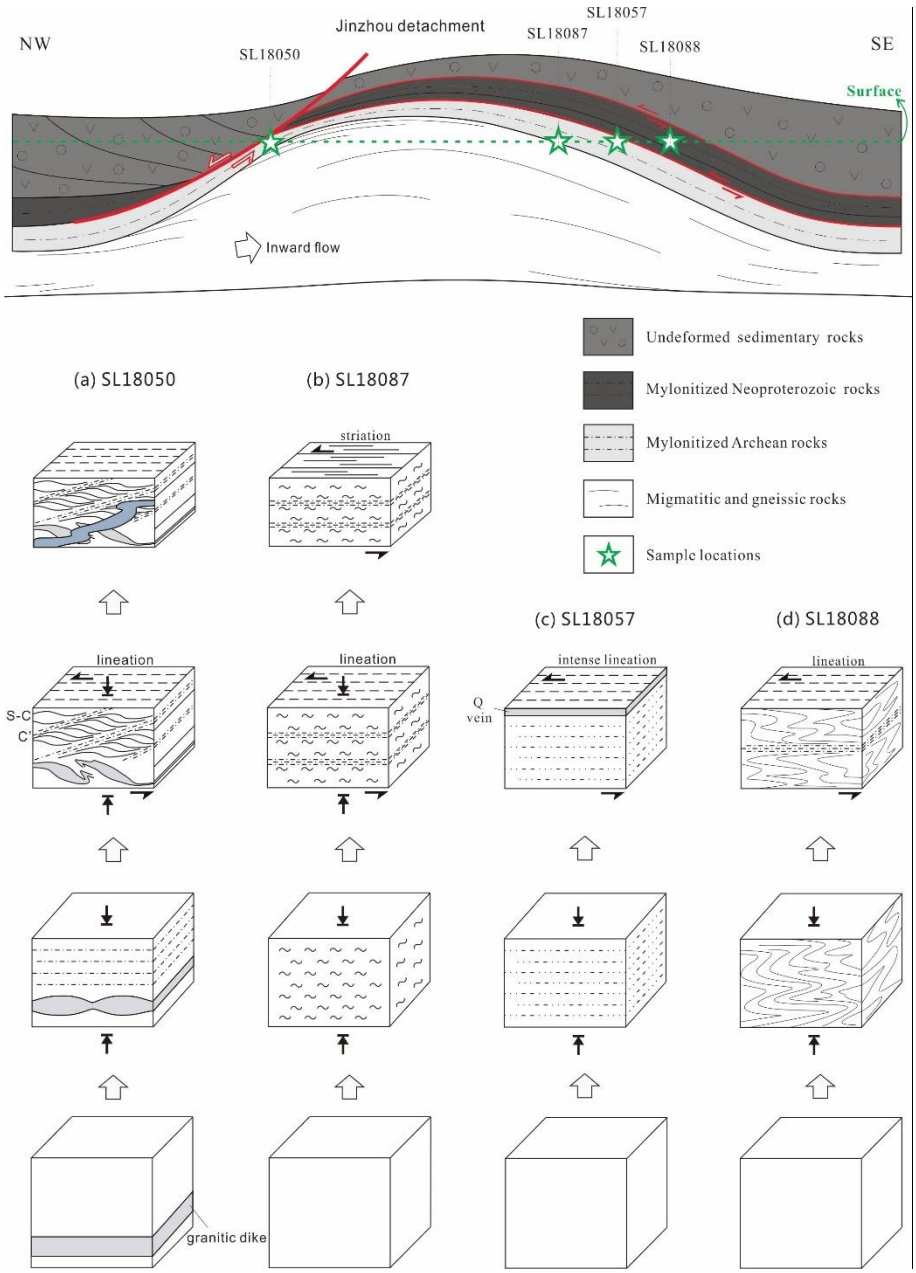

Figure 12. Cross-section of Liaonan MCC and graphic analysis of progressive shearing.
(a) Progressive mylonitization and the relationship between veins and foliations of SL18050 from JDFZ. (b) Progressive shearing (penetrative fish-shaped feldspar, discrete foliations and lineations, and striae) of SL18087 from DSZ. (c) Penetrative mylonitization and quartz veins with lineations of SL18057 from DSZ. (d) Intrafolial folds superposed by foliations and lineations of SL18088 from DSZ.

6.2 Timing of shearing and exhumation of JDFZ and DSZ

Geochronology of sheared rocks along JDFZ and syn-kinematic plutons of Liaonan MCC has been studied systematically to discuss the tectonic evolution and magmatic events during the exhumation of Liaonan MCC (e.g., Yin & Nie, 1996; Wu et al., 2005a, b; Yang et al., 2007; Ji et al., 2009, 2015; Ouyang et al., 2010; Lin et al.,

2011; Liu et al., 2011, 2013; Jiang et al., 2016). Shearing along the JDFZ initiated before ca. 134 Ma (Liu et al., 2013), followed by slow cooling and exhumation of the lower plate accompanied a giant magmatic event from 130 Ma to 120 Ma subsequently (Wu et al., 2005a, b; Guo, 2004; Ji et al., 2009, 2015). The post-kinematic emplacement of JDFZ is exemplified by the Zhaofang granodiorite pluton (113Ma; Ji et al., 2009) and a small granite-porphyry dike (115Ma; Jiang et al., 2016).

New zircon U-Pb age data of syn-kinematic dikes from DSZ in this paper constrain the crystallization ages to 134 Ma (SL17046) and 138 Ma (SLP1702), which are similar to those of the early syn-kinematic dikes along the JDFZ (134 Ma; Liu et al., 2013). The results, therefore, imply that both JDFZ and DSZ experienced identical early shearing at around 138-131 Ma. Subsequently, shearing continued in the JDFZ between 130Ma and 116 Ma, accompanied by intensive magmatic activities, which caused that most granitic magmas intruded into the JDFZ. The cessation of shearing along JDFZ is constrained at ca. 115Ma (Jiang et al., 2016).

General cooling paths of Liaonan MCC showed the lower plate of JDFZ was exhumed progressively and sequentially in two different stages (an early slow and a late rapid) of crustal extension (e.g., Charles et al., 2012; Liu et al., 2013). However, the data have never been discussed respectively in the JDFZ and DSZ. By combining the U-Pb data of syn-kinematic dikes (Ouyang et al., 2010; Liu et al., 2013; Jiang et al., 2016 and this paper) and the $^{40}Ar/^{39}Ar$ data on amphibole, muscovite, biotite and K-feldspar (Yin & Nie, 1996; Yang et al., 2007; Lin et al., 2011) along the JDFZ and DSZ, we construct the cooling paths in Figure 13. JH-70 and JH-67 are off-deviation (Figure 13), probably because JH-70 is located at the intersection of the two shear zones, and JH-67 is located closer to the core. It can be seen from the cooling path (Figure 13) that the two shear zones together suffered shearing in early the Cretaceous, and then the JDFZ experienced later rapid exhumation. Also, $^{40}Ar/^{39}Ar$ dating of biotite shows the age of exhumation along the DSZ is slightly earlier than the age along the JDFZ. Therefore, the JDFZ and DSZ have experienced an early uniform shearing and late inconsonant exhumation.

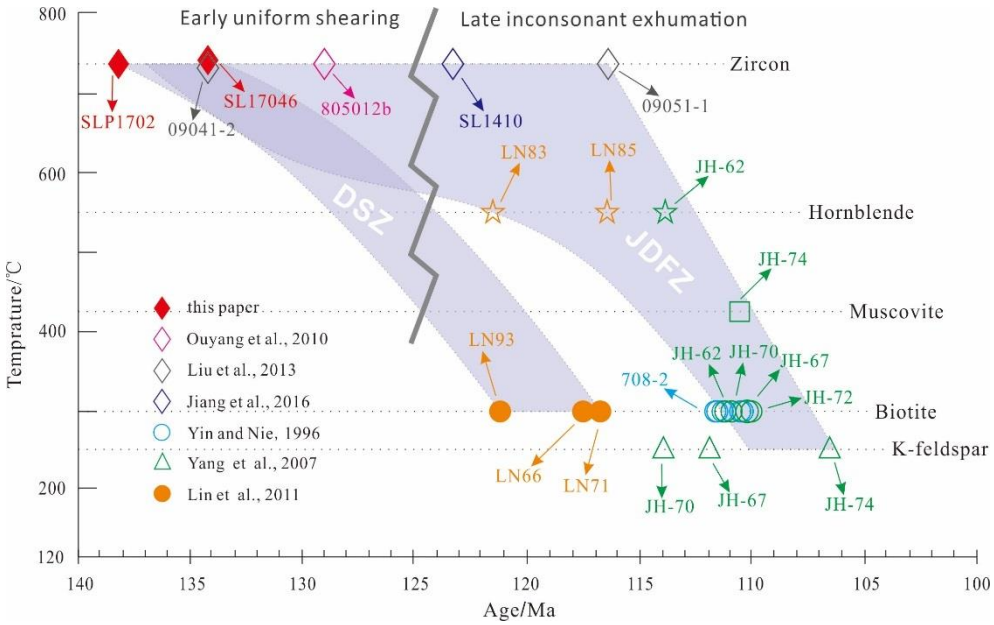

Figure 13. Cooling paths of the DSZ and the JDFZ.
Solid symbols: DSZ results; open symbols: JDFZ results.

6.3 Two-stage evolution of crustal extension in Liaonan MCC

6.3.1 Tangential shearing and doming

A general conclusion from regional stratigraphic studies is that the DSZ comprises a general younging sequence from Archean gneisses in Lower Unit, through Neoproterozoic layers at the Upper Unit, to the Cambrian rocks (Figure 11). A TDC between the Lower Unit and the Upper Unit marks a break in metamorphic grades in the stratigraphic sequence, but there is a gradual decrease in metamorphic grades from lower greenschist rocks in the lower Unit to non-metamorphosed sedimentary rocks in the upper Unit. Structural, metamorphic and geothermometrical analysis reveals that, due to intensive early Cretaceous shearing, the rocks were transformed into tectonites of highly sheared Archean gneisses (the Lower Unit, metamorphosed up to lower amphibolite facies) and sheared Neoproterozoic to lower Paleozoic meta-sedimentary rocks (the Upper Unit, metamorphosed up to lower greenschist facies). Deformation temperatures decrease from 630 °C and 470 °C in the Lower Unit to 350 °C in the Upper Unit. Structural, microstructural and fabric analysis shows that rocks beneath and above the TDC possess structures and fabrics of identical geometries and kinematics that are consistent with those along the JDFZ. The above results suggest that rocks on both sides of the TDC along the DSZ were sheared at the same time, but at different crustal levels, which is consistent with a tangential shearing system prevailing during the formation of the DSZ. Geochronological dating of syn-kinematic granite dikes from the DSZ (134Ma) is similar to the ages of shearing at the core (134Ma; Liu et al., 2013) and along the JDFZ (133Ma; Liu et al., 2013). The similar characteristics of mylonitization, identical kinematic indicators and the coeval shearing of JDFZ, DSZ and the core demonstrate that they experienced the early sub-horizontal or tangential shearing and

doming (Figure 14a) during an early stage of deformation in the Liaonan MCC.

6.3.2 Progressive shearing along the JDFZ and exhumation of the Liaonan MCC

As also shown in the above context, a typical sequence of tectonites are distributed along the JDFZ (Liu et al., 2005, 2013; Li et al., 2015). Relatively lower temperature superimposition structures and fabrics are well preserved in the tectonites, indicating progressive superimposition of late shearing on early deformation fabrics and gradual exhumation of middle and lower crustal rocks (Liu et al., 2005, 2013). On the other hand, a master detachment fault separates highly sheared rocks in the lower plate from undeformed sedimentary rocks in the upper plate, which contrasts the DSZ. Geochronological dating revealed that progressive shearing along the JDFZ terminated at ca. 113Ma when the undeformed post-kinematics dikes intruded into JDFZ (Ji et al., 2009). Identical kinematics of shearing along the JDFZ and the DSZ, i.e., consistent stretching lineations (striking to 110°-290°) and shearing indicators (top-to-the-WNW), demonstrate that the development of JDFZ is a continuation of early tangential shearing.

However, a dome-shaped structure is revealed for the present-day structural configuration of the Liaonan MCC. It is suggested that the domal configuration can be attributed to neither tangential shearing in the entire area nor detachment faulting along the JDFZ. A stage of doming is proposed to account for the occurrence of structural configuration. Could the sub-horizontal tangential shearing induce the doming? Various mechanisms have been proposed for the dynamic cause and kinematic development of domes (Whitney et al., 2004; Yin, 2004; Xu & Ma, 2015), including which these factors have the possibility on the premise of tangential shearing: (1) instability induced by vertical variation of viscosity (Yin, 2004), (2) stacking of anticline (Xu & Ma, 2015), and (3) isostatic compensation after the detachment of crustal extension (Brun et al., 1994; Tirel et al., 2004). Partial melting and magmatism may cause the low effective viscosity, which allows bulk vertical thinning of the crust, favoring exhumation processes (Platt et al., 2014). None of the above models is applicable, however, to the formation of the domal configuration of the Liaonan MCC. In this case, progressive tangential middle to lower crustal flow may induce small-scale perturbations, which give rise to fluctuation of the flow lines. As a result, deep rocks exhumed slowly by doming after high progressive strain accumulation (Figure 14b), which is compatible with a slow cooling and exhumation of the lower plate of the Liaonan MCC revealed by thermochronological studies (Liu et al., 2013).

Exhumation of the Liaonan MCC from early tangential shearing and doming to late detachment faulting is a progressive process in the unified extensional setting. In the process of gradual doming, strain was localized along the western limb of the MCCs that further evolved into the JDFZ. A fast rate of extension may have resulted in rapid cooling and exhumation of the lower plate due to detachment faulting along the JDFZ (Figure 14c; Liu et al., 2013). Brittle degradation and fragmentation are superimposed on the ductily sheared rocks and fabrics during progressive faulting

(Liu et al., 2005, 2011, 2013; Yang et al., 2007). Detachment faulting could be the primary mechanism of the final unroofing and the juxtaposition of formerly deep rocks and upper crustal rocks. In this case, a lower to middle crustal mylonitic zone, instead of a mylonitic front, occurs at the DSZ.

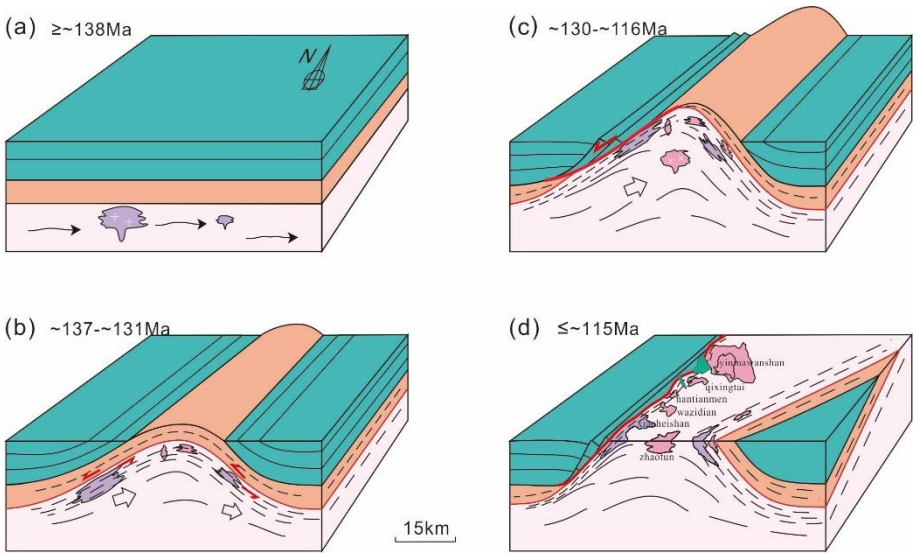

Figure 14. Evolution model of the Liaonan MCC associated with middle and lower crustal flow

(a) Onset of tangential shearing in the middle and lower crust before ca. 138Ma. (b) Intense tangential shearing induces doming. (c) JDFZ developed in the western part. (d) DSZ stopped shearing and large number of magmatic intruded the JDFZ.

Conclusions

(1) The DSZ encompasses highly sheared Archean gneisses metamorphosed up to lower amphibolite facies (Lower Unit) and sheared Neoproterozoic meta-sedimentary rocks of up to lower greenschist facies (Upper Unit, which were cut lost in JDFZ), showing identical geometries and kinematics that are consistent with those along the JDFZ.

(2) Zircons U-Pb ages from syn-kinematic granitic dikes from DSZ yields an age ca. 134 Ma, which is similar to the ages of early shearing along the JDFZ (ca. 133~134 Ma), implying the shearing initiated in both JDFZ and DFZ at the early stage.

(3) The exhumation of lower plate in the Cretaceous Liaonan MCC experienced two stages: (1) an early stage of slow exhumation due to tangential shearing and doming along the DSZ associated with middle and low crust flow, and (2) a late stage of fast exhumation via detachment faulting along the JDFZ.

Acknowledgments

This research was financially supported by the National Natural Science Foundation of China (41430211). We thank Weishi Chen at the Chinese Academy of Geological Sciences for support during fluid inclusion analysis. Fluid inclusions, EBSD and zircon dating data can be acquired from a permanent repository at OSF

(https://osf.io/csbwt/).

References

Bischoff, J.L. (1991). Densities of liquids and vapors in boiling NaCl-H2O solutions: A PVTX summary from 300 °C to 500 °C. *American Journal of Science*, 291, 309-338. doi:10.2475/ajs.291.4.309

Black, L.P., & Gulson, B.L. (1978). The age of the Mud Tank carbonatite, Strangways Range, Northern Territory. *BMR Journal of Australian Geology and Geophysics*, 3, 227-232. doi: 10.1007/BF00283322

Bodnar, R.J. (1983). A method of calculating fluid inclusion volumes based of vapor bubble diameters and P-V-T-X properties of inclusion fluids. *Economic Geology*, 78, 535-542. https://doi.org/10.2113/gsecongeo.78.3.535

Bodnar, R.J., & Vityk, M.O. (1994). Interpretation of microthermometric data for H_2O-NaCl fluid inclusions. In B.D. Vivo, & M.L. Frezzotti (eds.), Fluid Inclusions in Minerals, Methods and Appications (pp. 117-130), Blacksberg: Verginia Tech.

Brown, P.E. (1989). FLINCOR: A microcomputer program for the reduction and investigation of fluid-inclusion data. *American Mineralogist*, 74, 1390-1393.

Brun, J.P., Sokoutis, D., & Driessche, J.V.D. (1994). Analogue modeling of detachment fault systems and core complexes. *Geology*, 22, 319-322. doi:10.1130/0091-7613(1994)022<0319:AMODFS>2.3.CO;2

Buck, W.R. (1988). Flexural rotation of normal faults. *Tectonics*, 7, 959-973. doi:10.1029/tc007i005p00959

Cao, S.Y., Franz, N., Manfred, B., Liu, J.L., & Genser, J. (2013). Structures, microfabrics and textures of the Cordilleran-type Rechnitz metamorphic core complex, Eastern Alps. *Tectonophysics*, 608, 1201-1225. doi:10.1016/j.tecto.2013.06.025

Charles, N., Gumiaux, C., Augier, R., Chen, Y., Faure, M., Lin, W., & Zhu, R.X. (2012). Metamorphic core complex dynamics and structural development: Field evidences from the Liaodong Peninsula (China, East Asia). *Tectonophysics*, 560, 22–50. doi:10.1016/j.tecto.2012.06.019

Chen, X.Y., Liu, J.L., Weng, S.T., Kong, Y.L., Wu, W.B., Zhang, L.S., & Li, H.Y. (2016). Structural geometry and kinematics of the AilaoShan shear zone: Insights from integrated structural, microstructural, and fabric studies of the Yao Shan complex, Yunnan, Southwest China. *International Geology Review*, 58, 849–873. doi:10.1080/00206814.2015.1136572

Coney, P.J. (1980). Cordilleran metamorphic core complexes: An overview. *Geological Society of America Memoirs*, 153, 7-31. doi:10.1130/MEM153-p7

Cooper, F.J., Platt, J.P., Anczkiewicz, R., & Whitehouse, M.J. (2010). Footwall dip of a core complex detachment fault: Thermobarometric constraints from the northern Snake Range (Basin and Range, USA): *Journal of Metamorphic Geology*, 28, 997-1020. doi:10.1111/j.1525-1314.2010.00907.x

Cui, K.Y., Pang Q.B., & Xu, Y.K. (1986). Characteristics of ductile nappe structure in South Liaoning province. *Liaoning Journal of Geology*, 2, 45-66.

Darby, B.J., Davis, G.A., Zhang, X., Wu, F., Wilde, S., & Yang, J. (2004). The newly discovered Waziyu metamorphic core complex, Yiwulushan, western Liaoning Province, North China. *Earth Science Frontiers*, 11, 145-155. doi:1005-2321(2004)03-0145-11

Davis, G.A., & Zheng, Y.D. (2002). Metamorphic core complexes: Definition, types and tectonic setting. *Geological Bulletin of China*, 21, 185-192. doi:10.3969/j.issn.1671-2552.2002.04.001

Davis, G.H., & Coney, P.J. (1979). Geologic development of the Cordilleran metamorphic core complexes. *Geology*, 7, 120-124.

Fu, Z.R., Li, D.W., Li, X.F., & Wang, X.D. (1992). Ore control structure analysis of metamorphic core complex and detachment fault. Beijing: China University of Geosciences Press.

Guo, C.L., Wu, F.Y., & Yang, J.H. (2004). The extensional setting of the early Cretaceous magmatism in eastern China: Example from the Yinmawanshan pluton in southern Liaodong Peninsula. *Acta Petrologica Sinica*, 20, 1193-1204.

Hall, D.L., Sterner, S.M., & Bodnar, R.J. (1988). Freezing point depression of NaCl-KCl-H_2O solutions. *Economic Geology*, 83, 197-202.

Hong, Z.M. (1994). Crustal movements and structures on the northern margin of North China platform in the middle to late Proterozoic period. *Geology of Chemical Minerals*, 3, 145-153.

Ji, M., Liu, J.L., Hu, L., Guan, H.M., Davis, G.A., & Zhang, W. (2009). Zircon SHRIMP U-Pb age of Yinmawanshan and Zhaofang pluton in South Liaoning metamorphic core complex and its geological implications. *Acta Petrologica Sinica*, 1, 173-181. doi:1000-0569/2009/025(01)-0173-81

Ji, M. (2010). Early Cretaceous tectono-magmatic processes in the Liaodong Peninsula and regional tectonic implications, (Doctoral dissertation). Retrieved from CNKI. Beijing: China University of Geosciences.

Ji, M., Liu, J.L., Hu, L., Shen, L., & Guan, H.M. (2015). Evolving magma sources during regional tectonic extension: An example from the Liaonan metamorphic core complex and its implications on destruction of the North China Craton. *Tectonophysics*, 647, 48-62. doi:10.1016/j.tecto.2015.01.023

Jiang H., Liu J.L., Zhang J.Y., & Zheng Y.Y. (2016). The deformation of granitic rocks in the Jinzhou detachment fault zone, southern Liaoning: Microstructures, fabrics and geochronology analysis. *Acta Petrologica Sinica*, 32, 2707-2722. doi:1000-0569/2016/032(09)-2707-22

Kruckenberg, S.C., Whitney, D.L., Teyssier, C., Fanning, C.M. & Dunlap, W.J. (2008). Paleocene-Eocene migmatite crystallization, extension, and exhumation in the hinterland of the northern Cordillera: Okanogan dome, Washington, USA. *Geological Society of America Bulletin*, 120, 912-929. doi:10.1130/B26153.1

Law, R.D. (2014). Deformation thermometry based on quartz c-axis fabrics and recrystallization microstructures: A review. *Journal of structural geology*. 66, 129-161. doi:10.1016/j.jsg.2014.05.023

Law, R.D. (2015). Orogen-scale along-strike continuity in quartz recrystallization microstructures adjacent to the Main Central Thrust: Implications for

deformation temperatures, strain rates and flow stresses. *Geological Society of America Abstracts with Programs*, 47(7), 289.

Li, J.B., Lu, Y.H., & Jiang, Z.P. (2012). Strain and shear types of Liaonan Wanfu metamorphic core complex ductile shear zone. *Joumal of East China Institute of Technology (Natural Science)*, 35, 238-245.

Li, J.B., Guo, L., Ouyang, Z.X., Zeng, T., Ding, Y.J., & Zhang, Y. (2015). Strain and Kinematic Vorticity Analysis of the Liaonan Metamorphic Core Complex Ductile Detachment Zone. *Acta Scientiarum Naturalium Universitatis Pekinensis*, 51(6), 99-111. doi:10.13209/j.0479-8023.2015.111

Lin, W., Faure, M., Monie, P., Scharer, U., & Panis, D. (2008). Mesozoic extensional tectonics in Eastern Asia: The South Liaodong peninsula metamorphic core complex (NE China). *Journal of geology*, 116(2), 134-154. doi:10.1086/527456

Lin, W., Monié, P., Faure, M., Schärer, U., Shi, Y.H., Breton, N.L., & Wang, Q.C. (2011). Cooling paths of the NE China crust during the Mesozoic extensional tectonics: example from the south-Liaodong peninsula metamorphic core complex. *Journal of Asian Earth Sciences*, 42, 1048-1065. doi:10.1016/j.jseaes.2010.09.007

Lin, W., Faure, M., Chen, Y., Ji, W.B., Wu, L., Charles, N., & Wang, Q.C. (2013a). Late Mesozoic compressional to extensional tectonics in the Yiwulüshan massif, NE China and its bearing on the evolution of the Yinshan-Yanshan orogenic belt: Part I: Structural analyses and geochronological constraints. *Gondwana Research*, 23(1), 54-77. doi:10.1016/j.gr.2012.02.013

Lin, W., Charles, N., Chen, Y., Chen, K., Faure, M.,Wu, L., et al. (2013b). Late Mesozoic compressional to extensional tectonics in the Yiwulüshan massif, NE China and its bearing on the evolution of the Yinshan-Yanshan orogenic belt: Part II: Anisotropy of magnetic susceptibility and gravity modeling. *Gondwana Research*, 23(1), 78-94. doi:10.1016/j.gr.2012.02.012.

Lister, G.S., & Davis G.A. (1989). The origin of metamorphic core complexes and detachment faults formed during Tertiary continental extension in the northern Colorado River region, U.S.A. *Journal of Structural Geology*, 11, 65-94. doi:10.1016/0191-8141(89)90036-9

Liu, H.C., & Wu, Q.H. (2002). Characteristics of fluid inclusions in quartz veins in Xiaotian-Mozitan fault and their tectonic implications. *Geotectonic et Metallogenia*, 26(3), 67-73. doi:1001-1552(2002)03-290-07

Liu, J.L., Davis, G.A., Lin, Z.Y., & Wu, F.Y. (2005). The Liaonan metamorphic core complex, Southeastern Liaoning Province, North China: A likely contribution to Cretaceous rotation of Eastern Liaoning, Korea and contiguous areas. *Tectonophysics*, 407, 65-80. doi:10.1016/j.tecto.2005.07.001

Liu, J.L., Guan, H.M., Ji, M., & Hu, L. (2006). Late Mesozoic metamorphic core complexes: New constraints on lithosphere thinning in North China. *Progress in Natural Science*, 16, 633-638.

Liu, J.L., Ji, M., Shen, L., Guan, H.M., & Davis, G.A. (2011). Early Cretaceous extension in the Liaodong Peninsula: Structural associations, geochronological constraints and regional tectonic implications. *Science China Earth Science*,

54(6), 823-842, doi:10.1007/s11430-011-4189-y

Liu, J.L., Shen, L., Ji, M., Guan, H.M., Zhang, Z.C., & Zhao, Z.D. (2013). The Liaonan/Wanfu metamorphic core complexes in the Liaodong Peninsula: two stages of exhumation and constraints on the destruction of the North China Craton. *Tectonics*, 32, 1121-1141. doi:10.1002/tect.20064

Liu, J.L., Gan, H.N., Jiang, H., & Zhang, J.Y. (2016). Rheology of the middle crust under tectonic extension: Insights from the Jinzhou detachment fault zone of the Liaonan metamorphic core complex, eastern North China Craton. *Journal of Asian Earth Sciences*, 139, 61-70. doi:10.1016/j.jseaes.2016.12.024

Liu, Y.S., Hu, Z.C., Gao, S., Gunther, D., Xu, J., Gao, C.G., & Chen, H.H. (2008). In situ analysis of major and trace elements of anhydrous minerals by LA-ICP-MS without applying an internal standard. *Chemical Geology*, 257, 34-43. doi:10.1016/j.chemgeo.2008.08.004

Lu, H.Z. (1990). On fluid-melt inclusions. Beijing: Science Press.

Mizera, M., Little, T.A., Biemiller, J., Ellis, S., Webber, S., & Norton, K.P. (2019). Structural and geomorphic evidence for rolling-hinge style deformation of an active continental low-angle normal fault, SE Papua New Guinea. *Tectonics*, 38(5), 1556-1583.

Neumayr, P., Hoinkes, G., Puhl, J., Mogessie, A., & Khudeir, A.A. (1998). The Meatiq dome (Eastern Desert, Egypt) a Precambrian metamorphic core complex: Petrological and geological evidence. *Journal of Metamorphic Geology*, 16(2), 259-279. doi:10.1111/j.1525-1314.1998.00132.x

Norlander, B.H., Whitney, D.L., Teyssier, C., & Vanderhaeghe, O. (2002). Partial melting and decompression of the Thor-Odin dome, Shuswap metamorphic core complex, Canadian Cordillera. *Lithos*, 61, 103-125. doi:10.1016/S0024-4937(02)00075-0

Ni, J.L., Liu, J.L., Tang, X.L., Yang, H.B., & Guo, Q.J. (2013). The Wulian metamorphic core complex: A newly discovered metamorphic core complex along the Sulu orogenic belt, eastern China. *Journal of Earth Science*, 24(3), 297-313.

Ouyang, Z.X., Wang, T., Li, J.B., Guo, L., & Zeng, L.S. (2010). Deformation characteristics and zircon SHRIMP U-Pb age of the mylonitized granite vein in Jinzhou detachment fault of southern Liaoning: New evidence for constraint on the ductile detachment time. *Acta petrologica et mineralogica*, 4, 403-413.

Parrish, R.R., Carr, S.D., & Parkinson, D.L. (1988). Eocene extensional tectonics and geochronology of the southern Omineca Belt, British Columbia and Washington. *Tectonics*, 7, 181-212.

Passchier, C.W., & Trouw, R.A.J. (2005). Microtectonics. Berlin: Springer-Verlag.

Platt J.P., Behr, W.M. & Frances J.C. (2014). Metamorphic core complexes: windows into the mechanics and rheology of the crust. *Journal of the Geological Society*, 172(1), 9-27. doi:10.1144/jgs2014-036

Song, H.L. (1996). Characteristics of Fangshan Metamorphic core complex, Beijing and a discussion about its origin. *Journal of Graduate School, China University of Geosciences*, 2, 149-158.

Spencer, J.E. (1984). Role of tectonic denudation in warping and uplift of low-angle normal faults. *Geology*, 12(2), 95-98. doi:10.1130/0091-7613(1984)12<95:ROTDIW>2.0.CO;2

Stipp, M., Stuenitz, H., Heilbronner, R., & Schmid, S.M. (2002). The eastern Tonale fault zone: A natural laboratory for crystal plastic deformation of quartz over a temperature range from 250 to 700°C. *Journal of Structural Geology*, 24(12), 1861-1884. doi:10.1016/S0191-8141(02)00035-4

Teyssier, C., & Whitney, D.L. (2002). Gneiss domes and orogeny. *Geology*, 30(12), 139-1142. doi:10.1130/0091-7613(2002)030<1139:GDAO>2.0.CO;2

Tirel, C., Brun, J.P., & Burov, E. (2004). Thermomechanical modeling of extensional gneiss domes. *Geological Society of America Special Paper*, 380, 67-78, doi:10.1130/0-8137-2380-9.67

Vandenberg, L.C., & Lister, G.S. (1996). Structural analysis of basement tectonites from the Aegean metamorphic core complex of Los, Cyclades, Greece. *Journal of Structural Geology*, 18(12), 1437-1454. doi:10.1016/S0191-8141(96)00068-5

Vanderhaeghe, O., Teyssier, C., McDougal, I., & Dunlap, W.J. (2003). Cooling and exhumation of the Shuswap Metamorphic Core Complex constrained by $^{40}Ar/^{39}Ar$ thermochronology. *Geological Society of America Bulletin*, 115(12), 200–216. doi:10.1016/S0191-8141(96)00068-5

Wang, T., Zheng, Y.D., Zhang, J.J., Zeng, L.S., Donskaya, T., Guo, L., & Li, J.B. (2011). Pattern and kinematic polarity of late Mesozoic extension in continental NE Asia: Perspectives from metamorphic core complexes. *Tectonics*, 30, TC6007. doi:10.1029/2011TC002896

Wernicke, B., & Axen, G.J. (1988). On the role of isostasy in the evolution of normal fault systems. *Geology*, 16, 848-851. doi:10.1130/0091-7613(1988)016<0848:OTROII>2.3.CO;2

Whitney, D.L. (2004). Gneiss dome in orogeny. Boulder: Geological Society of America.

Whitney, D.L., Teyssier, C., Rey, P., & Buck, W.R. (2013). Continental and oceanic core complexes. *Geological Society of America Bulletin*, 125, 273-298. doi:10.1130/B30754.1

Wiedenbeck, M., Alle, P., Corfu, F., Griffin, W.L., Meier, M., Oberli, F., et al. (1995). Three Natural Zircon Standards for U-Th-Pb, Lu-Hf, Trace-Element and Ree Analyses. *Geostandards Newsletter*, 19(1), 1-23. doi:10.1111/j.1751-908X.1995.tb00147.x

Wiedenbeck, M., Hanchar, J.M., Peck, W.H., Sylvester, P., Valley, J., Whitehouse, M., Kronz, A., et al. (2004). Further characterisation of the 91500 zircon crystal. *Geostandards and Geoanalytical Research*, 28(1), 9-39. doi:10.1111/j.1751-908X.2004.tb01041.x

Wu, F.Y., Yang, J.H., Wilde, S.A., & Zhang, X.O. (2005a). Geochronology, petrogenesis and tectonic implications of Jurassic granites in the Liaodong Peninsula, NE China. *Chemical Geology*, 221, 127-156. doi:10.1016/j.chemgeo.2005.04.010

Wu, F.Y., Lin, J.Q., Wilde, S.A., Zhang, X.O., & Yang, J.H. (2005b). Nature and

966 significance of the Early Cretaceous giant igneous event in eastern China. *Earth*
967 *and Planetary Science Letters*, 233, 103-119. doi:10.1016/j.epsl.2005.02.019
968 Xu, Z.Q., and Ma, X.X., 2015, The Chinese Phanerozoic gneiss domes:
969 Subduction-related type, collision-related type and combination type of
970 subduction-collision. *Acta Petrologica Sinica*, 31(12), 3509-3523.
971 Xu, Z.Q., Li, H., Wang, Z., & Li, D. (1991). Crustal contraction and extension in
972 Southern Liaoning. *Geological Review*, 37, 193-202.
973 Yang, J.H., Wu, F.Y., Chung, S.L., Lo, C.H., Wilde, S.A., & Davis, G.A. (2007).
974 Rapid exhumation and cooling of the Liaonan metamorphic core complex:
975 Inferences from $^{40}Ar/^{39}Ar$ thermochronology and implications for Late Mesozoic
976 extension in the eastern North China Craton. *Geological Society of America*
977 *Bulletin*, 119, 1405-1414. doi:10.1130/B26085.1
978 Yang, J.H., Wu, F.Y., Chung, S.L., & Lo, C.H. (2008). The extensional geodynamic
979 setting of Early Cretaceous granitic intrusions in the eastern North China Craton:
980 evidence from laser ablation $^{40}Ar/^{39}Ar$ dating of K-bearing minerals. *Acta*
981 *Petrologica Sinica*, 24, 1175-1184.
982 Yang, Z.S. (1985). Ductile shear zone and Archean complex. *Journal of Changchun*
983 *University of Earth Sciences*, 15, 1-12.
984 Yang, Z.Z., Meng, Q., Gang, J., & Han, X. (1996). The metamorphic core complex
985 structure in south Liaoning. *Liaoning Geology*, 13, 241-250.
986 Yin, A., & Nie, S.Y. (1996). A Phanerozoic palinspastic reconstruction of China and
987 its neighboring regions. In A. Yin, & T.A. Harrison (Eds.), The Tectonic
988 Evolution of Asia (pp. 442-485). New York: Cambridge University Press.
989 Yin, A. (2004). Gneiss domes and gneiss dome systems, in D.L. Whitney, C. Teyssier,
990 C.S. Siddoway (eds.), Gneiss domes in orogeny: Boulder (Vol. 380, pp. 1-14).
991 Colorado: Geological Society of America Special Paper.
992 Zheng, Y.D, Wang, S.Z, & Wang, Y.F. (1990). An enormous thrust nappe and
993 extensional metamorphic core complex newly discovered in Sino-Mongolian
994 boundary area. *Science China*, 9, 1145-1154.